Article

Cancer Cell

Transcriptional Dependencies in Diffuse Intrinsic Pontine Glioma

Graphical Abstract

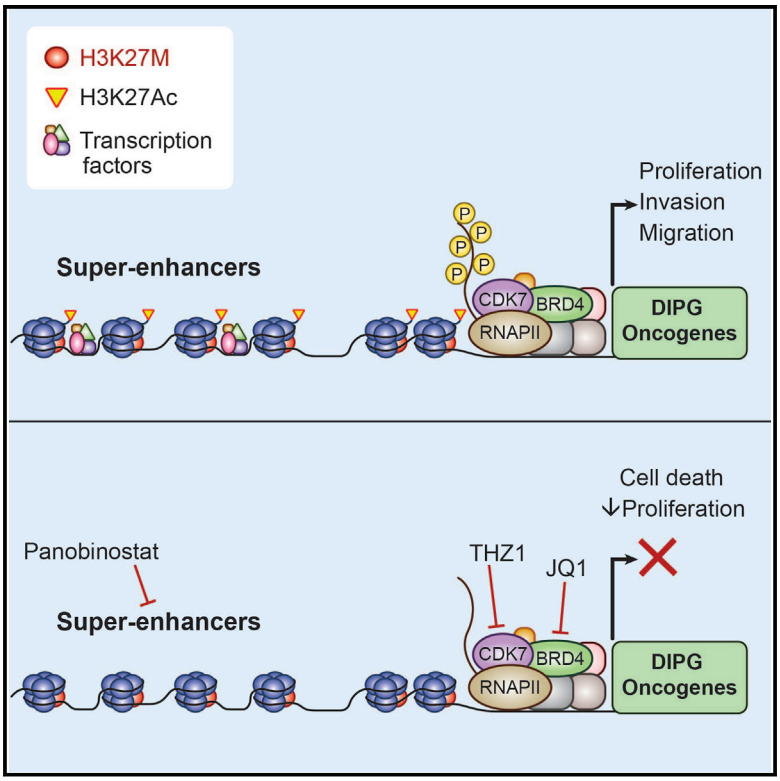

Highlights

- DIPG is vulnerable to transcriptional disruption via BRD4 or CDK7 blockade
- Panobinostat-resistant DIPG cells retain susceptibility to CDK7 blockade with THZ1
- Super-enhancer analyses indicate an early oligodendroglial precursor cell of origin
- Chromatin analyses reveal EPH receptor signaling as crucial to DIPG invasion

Authors

Surya Nagaraja, Nicholas A. Vitanza, Pamelyn J. Woo, ..., Joanna Wysocka, Yujie Tang, Michelle Monje

Correspondence

yujietang@shsmu.edu.cn (Y.T.), mmonje@stanford.edu (M.M.)

In Brief

Nagaraja et al. show that diffuse intrinsic pontine glioma (DIPG), a fatal pediatric tumor, is vulnerable to BRD4 or CDK7 blockade, and inhibition of either synergizes with HDAC inhibition to block growth of DIPG. Super-enhancer analysis of DIPG suggests oligodendroglial precursors as the cell of origin.

Nagaraja et al., 2017, Cancer Cell *31*, 1–18
May 8, 2017
http://dx.doi.org/10.1016/j.ccell.2017.03.011

CellPress

Please cite this article in press as: Nagaraja et al., Transcriptional Dependencies in Diffuse Intrinsic Pontine Glioma, Cancer Cell (2017), http://dx.doi.org/10.1016/j.ccell.2017.03.011

Cancer Cell
Article

CellPress

Transcriptional Dependencies in Diffuse Intrinsic Pontine Glioma

Surya Nagaraja,[1] Nicholas A. Vitanza,[1] Pamelyn J. Woo,[1] Kathryn R. Taylor,[1] Fang Liu,[2] Lei Zhang,[2] Meng Li,[2] Wei Meng,[3] Anitha Ponnuswami,[1] Wenchao Sun,[1] Jie Ma,[3] Esther Hulleman,[4] Tomek Swigut,[5] Joanna Wysocka,[5,6,7,8] Yujie Tang,[1,2,3,*] and Michelle Monje[1,6,9,*]

[1]Department of Neurology, Stanford University, Palo Alto, CA 94305, USA
[2]Key Laboratory of Cell Differentiation and Apoptosis of National Ministry of Education, Department of Pathophysiology, Shanghai Jiao Tong University School of Medicine, 280 South Chongqing Road, Shanghai 200025, P.R. China
[3]Department of Pediatric Neurosurgery, Xin Hua Hospital Affiliated to Shanghai Jiao Tong University School of Medicine, Shanghai 200092, P.R. China
[4]Department of Pediatric Oncology, VU University Medical Center, 1081 HV Amsterdam, the Netherlands
[5]Department of Chemical and Systems Biology, Stanford University, Palo Alto, CA 94305, USA
[6]Institute for Stem Cell Biology and Regenerative Medicine, Stanford University, Palo Alto, California 94305, USA
[7]Department of Developmental Biology, Stanford University, Palo Alto, California 94305, USA
[8]Howard Hughes Medical Institute, Stanford School of Medicine, Stanford University, Palo Alto, California 94305, USA
[9]Lead Contact
*Correspondence: yujietang@shsmu.edu.cn (Y.T.), mmonje@stanford.edu (M.M.)
http://dx.doi.org/10.1016/j.ccell.2017.03.011

SUMMARY

Diffuse intrinsic pontine glioma (DIPG) is a fatal pediatric cancer with limited therapeutic options. The majority of cases of DIPG exhibit a mutation in histone-3 (H3K27M) that results in oncogenic transcriptional aberrancies. We show here that DIPG is vulnerable to transcriptional disruption using bromodomain inhibition or CDK7 blockade. Targeting oncogenic transcription through either of these methods synergizes with HDAC inhibition, and DIPG cells resistant to HDAC inhibitor therapy retain sensitivity to CDK7 blockade. Identification of super-enhancers in DIPG provides insights toward the cell of origin, highlighting oligodendroglial lineage genes, and reveals unexpected mechanisms mediating tumor viability and invasion, including potassium channel function and EPH receptor signaling. The findings presented demonstrate transcriptional vulnerabilities and elucidate previously unknown mechanisms of DIPG pathobiology.

INTRODUCTION

Diffuse intrinsic pontine glioma (DIPG) is a universally fatal CNS cancer representing the leading cause of brain tumor-related death in children (Ostrom et al., 2015). As complete resection is not possible and conventional chemotherapy is ineffective, the standard of care remains radiation alone. Recent genomic studies have revealed that ~80% of DIPG tumors exhibit a characteristic mutation of lysine 27 to methionine (K27M) in genes encoding histone H3.3 and H3.1 and subsequent aberrant transcription (Bender et al., 2013; Chan et al., 2013; Khuong-Quang et al., 2012; Lewis et al., 2013; Schwartzentruber et al., 2012; Taylor et al., 2014; Wu et al., 2012). The H3K27M mutation results in perturbation of Polycomb repressive complex 2 (PRC2) function, resulting in global hypomethylation of K27 in all H3 variants (Lewis et al., 2013; Bender et al., 2013; Wu et al., 2012) and broad epigenetic dysregulation believed to be central to DIPG oncogenesis (Bender et al., 2013; Chan et al., 2013; Lewis et al., 2013; Venneti et al., 2013; Funato et al., 2014).

We previously identified panobinostat, a multiple histone deacetylase (HDAC) inhibitor, as an effective agent against patient-derived DIPG cell cultures and xenograft models (Grasso et al., 2015). Panobinostat restored H3K27me3 (Grasso et al., 2015), likely via disruption of aberrant PRC2 inhibition through

Significance

Diffuse intrinsic pontine glioma (DIPG) is a universally fatal pediatric cancer. A histone-3 K27M mutation affects ~80% of DIPGs and drives aberrant transcription. Here, we demonstrate that transcriptional disruption achieved by targeting either BRD4 or CDK7 is a promising strategy for DIPG, particularly in combination with HDAC inhibition. Analyses of key regulatory elements called super-enhancers in DIPG underscores cell-identity genes, supporting the hypothesis that DIPG arises from a precursor cell in the oligodendroglial lineage and highlighting several unexpected gene families that prove functionally important to DIPG pathobiology. Taken together, the findings presented here identify targets for therapy of this devastating cancer.

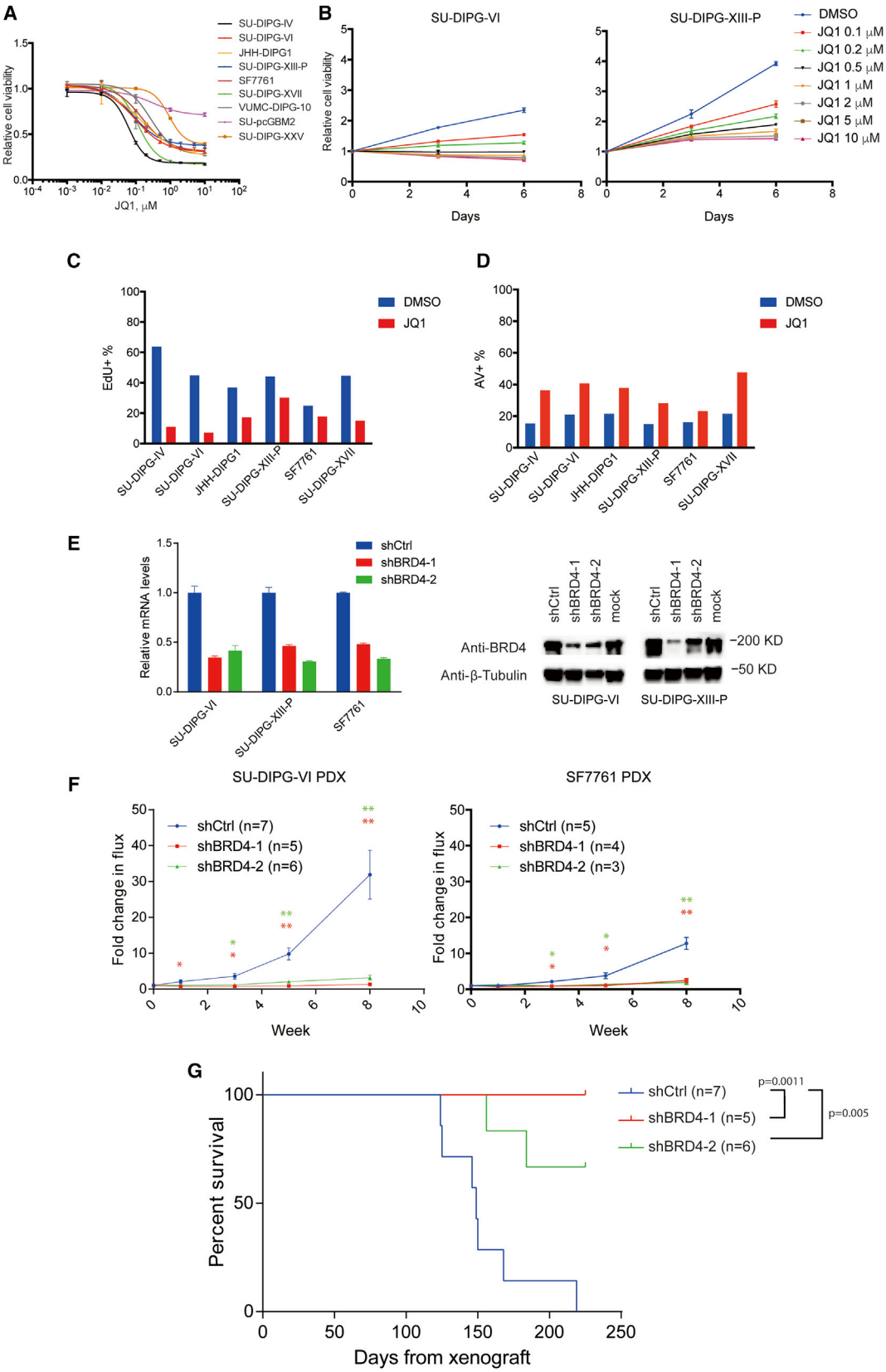

(legend on next page)

polyacetylation of nearby residues and subsequent blockade of K27M-PRC2 interactions (Brown et al., 2014). Large transcriptional changes were observed with panobinostat treatment, including rescue of many gene expression aberrations associated with the K27M mutation (Grasso et al., 2015). However, DIPG resistance to HDAC inhibition ultimately develops (Grasso et al., 2015), highlighting the importance of advancing drug combinations or identifying alternative strategies to more potently disrupt oncogenic gene expression.

An effective strategy in many preclinical models of malignancy with transcriptional dysregulation has been to disrupt efficient RNA polymerase II (RNAPII) transcription through inhibition of chromatin readers and writers (Posternak and Cole, 2016; Hagenbuchner and Ausserlechner, 2016). This has commonly been done through BET (bromodomain and extra-terminal) protein inhibition, targeting family member BRD4 (Lovén et al., 2013; Delmore et al., 2011; Dawson et al., 2011; Filippakopoulos and Knapp, 2014; Mertz et al., 2011; Zuber et al., 2011; Coudé et al., 2015; Picaud et al., 2015; Sengupta et al., 2015a, 2015b; Shahbazi et al., 2016; Zhang et al., 2016; Bid et al., 2016), a key activator of RNAPII transcription at active chromatin marks (Jang et al., 2005; LeRoy et al., 2008; Rahman et al., 2011). An alternative target is CDK7, a member of the cyclin-dependent kinase family involved in regulation of RNAPII phosphorylation, controlling transcriptional initiation, pausing, and elongation (Fisher and Morgan, 1994; Glover-Cutter et al., 2009; Larochelle et al., 2007, 2012; Rossignol et al., 1997; Serizawa et al., 1995). THZ1 is a highly specific CDK7 inhibitor effective in preclinical models for malignancies with transcription factor dysregulation, such as T cell acute lymphoblastic leukemia (Kwiatkowski et al., 2014), small cell lung carcinoma (Christensen et al., 2014), neuroblastoma (Chipumuro et al., 2014), and triple-negative breast cancer (Wang et al., 2015). In this study, we investigate the efficacy of single and combinatorial targeting of transcription in DIPG, and characterize gene expression and active chromatin elements, in an effort to identify core genes regulating DIPG oncogenesis.

RESULTS

Bromodomain Inhibition Disrupts In Vitro DIPG Cell Viability and In Vivo Tumor Growth

JQ1, a tool compound, is a thoroughly studied inhibitor of bromodomain activity with efficacy in a number of preclinical models (Filippakopoulos and Knapp, 2014; Mertz et al., 2011; Zuber et al., 2011; Bid et al., 2016; Coudé et al., 2015; Picaud et al., 2015; Sengupta et al., 2015a, 2015b; Shahbazi et al., 2016; Zhang et al., 2016). Many of the cancers studied to date that demonstrate sensitivity to transcriptional disruption exhibit *MYC* or *MYCN* amplification or overexpression. A subset of DIPGs exhibits *MYC/MYCN* amplification, with *MYCN* amplification observed chiefly in tumors that do not exhibit the H3K27M mutation and *MYC* amplification observed in H3K27M mutant tumors (Buczkowicz et al., 2014). A larger subset exhibits high levels of *MYC/MYCN* expression (Grasso et al., 2015; Figure S1A). However, transcriptional dysregulation in DIPG is chiefly driven by the H3K27M mutation (Bender et al., 2013; Chan et al., 2013; Lewis et al., 2013; Venneti et al., 2013; Funato et al., 2014). Given this well-established aberrancy, we hypothesized that DIPG may be vulnerable to transcriptional disruption. Eight patient-derived DIPG cultures and one pediatric cortical glioblastoma culture (SU-pcGBM2) were used in this study; seven of the eight DIPGs exhibit the H3K27M mutation and one is histone wild-type (WT) (H3.3K27M: SU-DIPG-VI, SU-DIPG-XIII-P, SU-DIPG-XVII, SU-DIPG-XXV, SF7761, and JHH-DIPG1; H3.1K27M: SU-DIPG-IV; H3WT and *MYCN* amplified: VUMC-DIPG-10; Tables S1 and S2). SU-pcGBM2 is histone-3 WT and exhibits a *TP53* mutation and *EGFR* amplification (Table S1; Venkatesh et al., 2015). To confirm and extend the observation that BET inhibition reduces DIPG cell viability (Taylor et al., 2015), we treated these patient-derived cell cultures with a range of concentrations of JQ1 and observed a dose-dependent reduction in DIPG cell viability across all cell cultures, particularly at later time points (72-hr half-maximal inhibitory concentration [IC_{50}] > 1 μM in most cultures; 6-day IC_{50} median 0.35 μM, range 0.076–2.06 μM; Figures 1A and S1B). Interestingly, while the H3WT culture VUMC-DIPG-10 responded to JQ1 treatment similarly to other DIPG cultures, the H3WT pediatric glioblastoma cell culture SU-pcGBM2 showed minimal vulnerability to JQ1 treatment (Figure 1A). While few conclusions can be drawn from the limited number of H3WT DIPG cultures available for study, H3WT DIPGs may be vulnerable to transcriptional disruption when carrying an *MYC/MYCN* amplification, whereas H3K27M DIPGs harbor sensitivity due to the H3K27M oncogenic effect on transcription. Time-course tracking of JQ1-treated DIPG cells indicated that the inhibitory effect of JQ1 against DIPG cells is more cytostatic than cytocidal (Figures 1B and

Figure 1. BRD4 Inhibition Inhibits DIPG Growth In Vitro and In Vivo

(A) Patient-derived DIPG cultures and pediatric GBM culture SU-pcGBM2 treated with JQ1 as indicated for 6 days. Cell viabilities normalized to 0.1% DMSO control values (n = 3 wells per data point).

(B) DIPG cells treated with JQ1 at indicated concentrations or 0.1% DMSO control. Cell viabilities measured at 0, 3, and 6 days of treatment and normalized to day-0 values (n = 3 wells per data point).

(C) 5-Ethynyl-2′-deoxyuridine (EdU) incorporation of DIPG cells treated with 0.1% DMSO or 1 μM JQ1 for 48 hr.

(D) Annexin V (AV)/DAPI staining of DIPG cells treated with 0.1% DMSO or 1 μM JQ1 for 72 hr.

(E) DIPG cells infected either of two clones of shBRD4 (shBD4-1 or shBRD4-2) or control construct (shCtrl) lentivirus. Knockdown efficiency by qRT-PCR (left, n = 2) or western blot (right).

(F) SU-DIPG-VI cells (left) and SF7761 cells (right) infected with lentivirus expressing shBRD4-1, shBRD4-2, or shCtrl (control) were implanted in the brainstem at P2 and allowed to engraft for 4 weeks. Tumor growth of DIPG xenografts were then monitored by IVIS (in vivo imaging system) imaging at weeks 0, 1, 3, 5, and 8. For SU-DIPG-VI: shCtrl n = 7 mice, shBRD4-1 n = 5 mice, shBRD4-2 n = 6 mice. For SF7761: shCtrl n = 5 mice, shBRD4-1 n = 4 mice, shBRD4-2 n = 3 mice. Data shown normalized to week-0 value for each group; error bars denote SEM. *p < 0.5, **p < 0.01 (two-tailed Student's t test).

(G) Survival curves of xenografted mice implanted with SU-DIPG-VI cells infected with lentivirus expressing shBRD4-1, shBRD4-2, or shCtrl construct. Log-rank analyses were performed to calculate the p value comparing shCtrl and shBRD4 groups (shCtrl n = 7 mice, shBRD4-1 n = 5 mice, shBRD4-2 n = 6 mice).

Data are shown as mean ± SD unless otherwise indicated. FACS analyses shown in bar plots (C and D) illustrate one representative experiment. See also Figure S1 and Tables S1–S3.

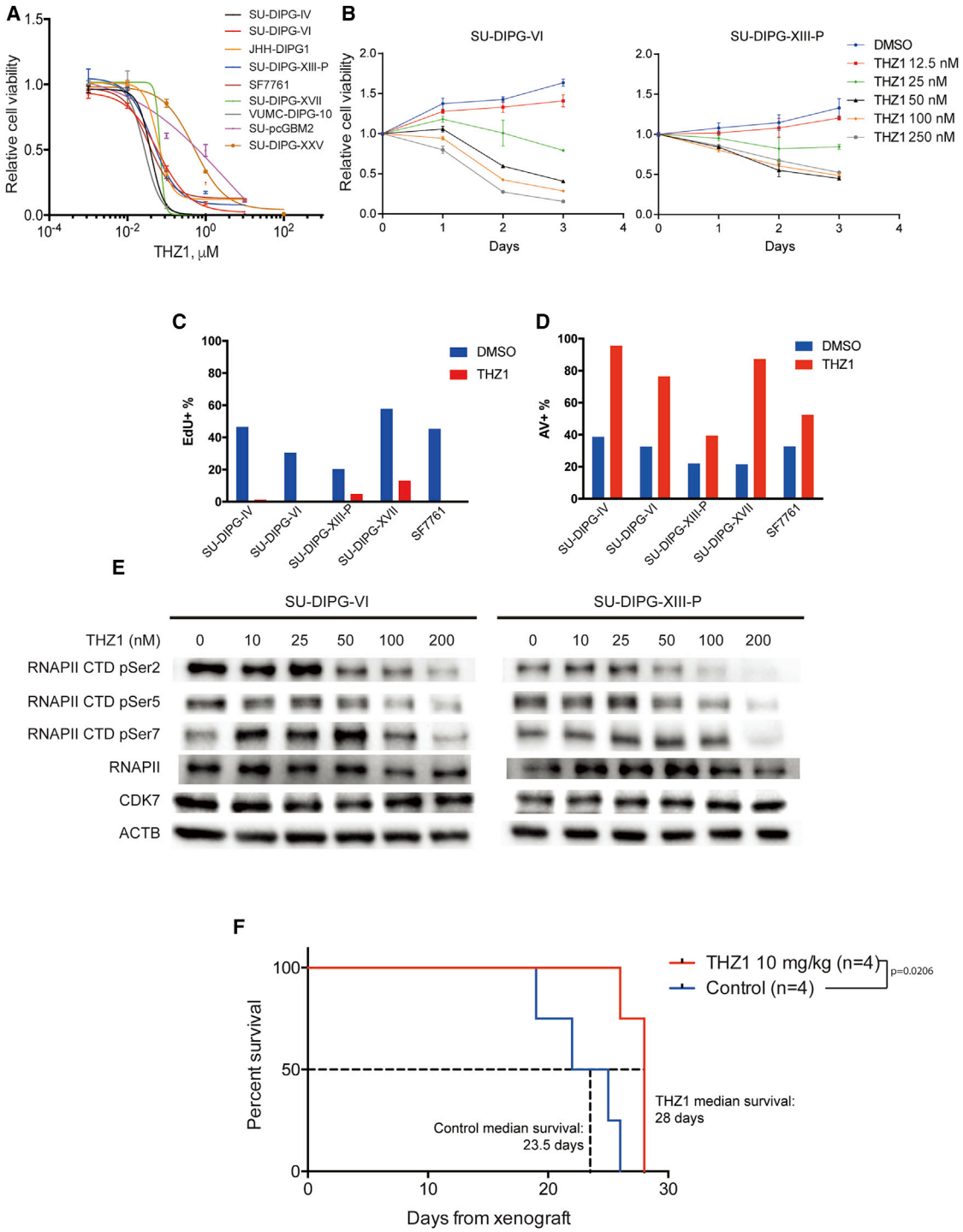

Figure 2. CDK7 Inhibitor THZ1 Disrupts DIPG Growth

(A) Patient-derived DIPG cultures (SU-DIPG-IV, SU-DIPG-VI, JHH-DIPG1, SU-DIPG-XIII-P, SF7761, SU-DIPG-XVII, VUMC-DIPG-10, SU-DIPG-XXV) and SU-pcGBM2 treated with THZ1 as indicated for 72 hr. Cell viabilities normalized to 0.1% DMSO control values (n = 3 wells per data point).

(B) SU-DIPG-VI and SU-DIPG-XIII-P cells treated with THZ1 at indicated concentrations or 0.1% DMSO control. Cell viabilities measured at 0, 1, 2, and 3 days of treatment and normalized to day-0 values (n = 3 wells per data point).

(C) EdU incorporation by DIPG cells treated with 0.1% DMSO or 0.1 μM THZ1 for 20 hr.

(D) Annexin V (AV)/DAPI staining of DIPG cells treated with 0.1% DMSO or 0.1 μM THZ1 for 48 hr.

(E) SU-DIPG-VI and SU-DIPG-XIII-P cells treated with THZ1 as indicated for 24 hr. Western blot analyses for phosphorylation levels at Ser2, Ser5, and Ser7 of RNA polymerase II C-terminal domain (RNAPII CTD). Total levels of RNAPII, CDK7, and β-actin (ACTB) also measured as control.

(legend continued on next page)

S1C). Indeed, fluorescence-activated cell sorting (FACS) analyses showed inhibition of cell proliferation (Figure 1C) and only a moderate increase in apoptosis following JQ1 exposure (Figure 1D).

We next tested the effect of bromodomain inhibitor drugs presently in clinical development, iBET762 (Mirguet et al., 2013) and OTX015 (Coudé et al., 2015). At 72 hr of treatment, DIPG cells largely demonstrated IC_{50} values greater than 1 μM, suggesting that these drugs are not sufficiently potent for clinical translation, but showed a modest dose-dependent inhibition of cell viability at 6 days of treatment (Figures S1D and S1E). Brain penetration studies indicated that OTX015 levels achieved in brain (~150 nM; Table S3) following standard in vivo dosing are only a fraction of the 72-hr IC_{50} for DIPG cells. While these relatively high IC_{50} values and insufficient brain penetration indicate that these specific agents lack the potency necessary for clinical translation in DIPG, the data suggest that DIPG cells may be sensitive to loss of bromodomain activity in principle.

To determine the therapeutic potential of effective bromodomain inhibition, we tested the effects of BRD4 loss in DIPG orthotopic xenograft models. Patient-derived DIPG cell cultures expressing firefly luciferase, SU-DIPG-VI-luc and SF7761-luc (Grasso et al., 2015; Hashizume et al., 2014), were infected with a vector expressing either short hairpin RNA (shRNA) targeting BRD4 or a non-targeting control (Figure 1E). BRD4 knockdown resulted in decreased proliferation and slowed DIPG cell growth in vitro, and did not alter luciferase expression or in vivo engraftment (Figures S1F–S1I). Accordingly, mice xenografted with DIPG cells expressing BRD4 shRNA showed a stark reduction in tumor growth and improved survival relative to mice xenografted with cells expressing the non-targeting control (Figures 1F and 1G). BRD4 function thus appears to be necessary for DIPG growth in vivo, underscoring the potential that effective bromodomain inhibition holds for DIPG therapy when appropriate pharmacological agents become available.

CDK7 Inhibition with THZ1 Impairs DIPG Growth

We next sought to determine whether alternative methods of disrupting transcription could be effective in DIPG. We found that THZ1 robustly reduced DIPG cell viability in a dose-dependent manner, with a median 72-hr IC_{50} of 56 nM in eight patient-derived DIPG cell cultures tested (range 28–533 nM) (Figures 2A, 2B, and S2A), consistent with IC_{50} concentrations reported in other malignant models (Christensen et al., 2014; Jiang et al., 2016). Similar to bromodomain inhibition, the SU-pcGBM2 culture was somewhat less vulnerable to CDK7 inhibition (IC_{50} 640 nM). Patient-derived DIPG cells exhibited robustly decreased proliferation (Figure 2C) and increased apoptosis (Figure 2D) following THZ1 exposure. Consistently, we observed loss of RNAPII CTD phosphorylation 24 hr after THZ1 treatment (Figure 2E), indicating effective CDK7 inhibition. Disruption of RNAPII transcription through CDK7 inhibition thus appears to potently disrupt DIPG cell viability.

To determine whether THZ1 could be used for brain tumors, we quantified brain penetration and observed an average THZ1 brain parenchymal concentration of 13.7 ng/g or approximately 24 nM following intraperitoneal dosing, and approximately 600 nM following intravenous dosing (Table S3). Given the relative potency of the agent against DIPG, we tested the efficacy of THZ1 in two patient-derived orthotopic xenograft models, SU-DIPG-VI and SU-DIPG-XIII-FL (derived from the frontal lobe DIPG metastasis in subject SU-DIPG-XIII). Our ability to administer THZ1 intravenously was limited by tail-vein sclerosis to only 1 week, but we observed proof-of-principle reduction in DIPG xenograft growth (Figure S2B). Similar to epigenetic modifying agents studied in previous publications (Tang et al., 2014; Grasso et al., 2015), we observed an increase in relative luciferase activity with in vitro THZ1 treatment (Figure S2C), suggesting that our in vivo observation of reduced luciferase levels was not due to a reduction in transcription of luciferase but rather to a decrease in tumor burden.

Next, we turned to intraperitoneal dosing of THZ1 in a particularly aggressive patient-derived DIPG xenograft model (SU-DIPG-XIII-P*). THZ1 administration resulted in a significant but modest (~20%) increase in median survival when compared with vehicle-treated control mice (Figure 2F). Taken together, these data suggest that DIPG is vulnerable to CDK7 inhibition both in vitro and in vivo, with better brain tissue delivery required for optimal clinical translation.

Combinatorial Transcriptional Therapy in DIPG

Our previous work showed that the Food and Drug Administration-approved drug panobinostat exhibits a degree of preclinical benefit against DIPG (Grasso et al., 2015), and it is presently in a phase I clinical trial for children with DIPG (NCT02717455). A recent study similarly demonstrated a modest benefit of panobinostat in a murine DIPG model evidenced by reduced tumor cell proliferation (Hennika et al., 2017). We hypothesized that stronger disruption of DIPG cell viability may come from combinatorial treatment with both HDAC inhibition and disruption of RNAPII-dependent transcription. HDAC inhibition together with JQ1 or THZ1 synergistically reduced cell viability across multiple DIPG cell cultures (Figures 3A, 3B, S3A, and S3B), and proved more effective in inhibiting proliferation and inducing apoptosis (Figures S3D and S3E). Synergistic inhibition of cell viability with JQ1 and THZ1 combinatorial treatment was also observed (Figure S3C).

As treatment with panobinostat ultimately results in resistance (Grasso et al., 2015), we hypothesized that transcription in these resistant cells may be disrupted through bromodomain or CDK7 inhibition. We generated panobinostat-resistant cells as previously described (Grasso et al., 2015) and found that panobinostat-resistant cells retained submicromolar sensitivity to THZ1 (Figure 3C). In contrast, cells resistant to panobinostat also

(F) SU-DIPG-XIII-P* cells were xenografted to the pons at postnatal day 43 (P43) and allowed to engraft for 10 days prior to treatment. SU-DIPG-XIII-P* represents a particularly aggressive subclone of the SU-DIPG-XIII-P culture. Mice were treated with THZ1 at 10 mg/kg intraperitoneally twice daily. Log-rank analyses were performed to calculate the p value, comparing vehicle-treated and THZ1-treated groups (vehicle n = 4 mice, THZ1 n = 4 mice).

Data are shown as mean ± SD unless otherwise indicated. FACS analysis shown in bar plots (C and D) for one representative experiment. See also Figure S2 and Table S3.

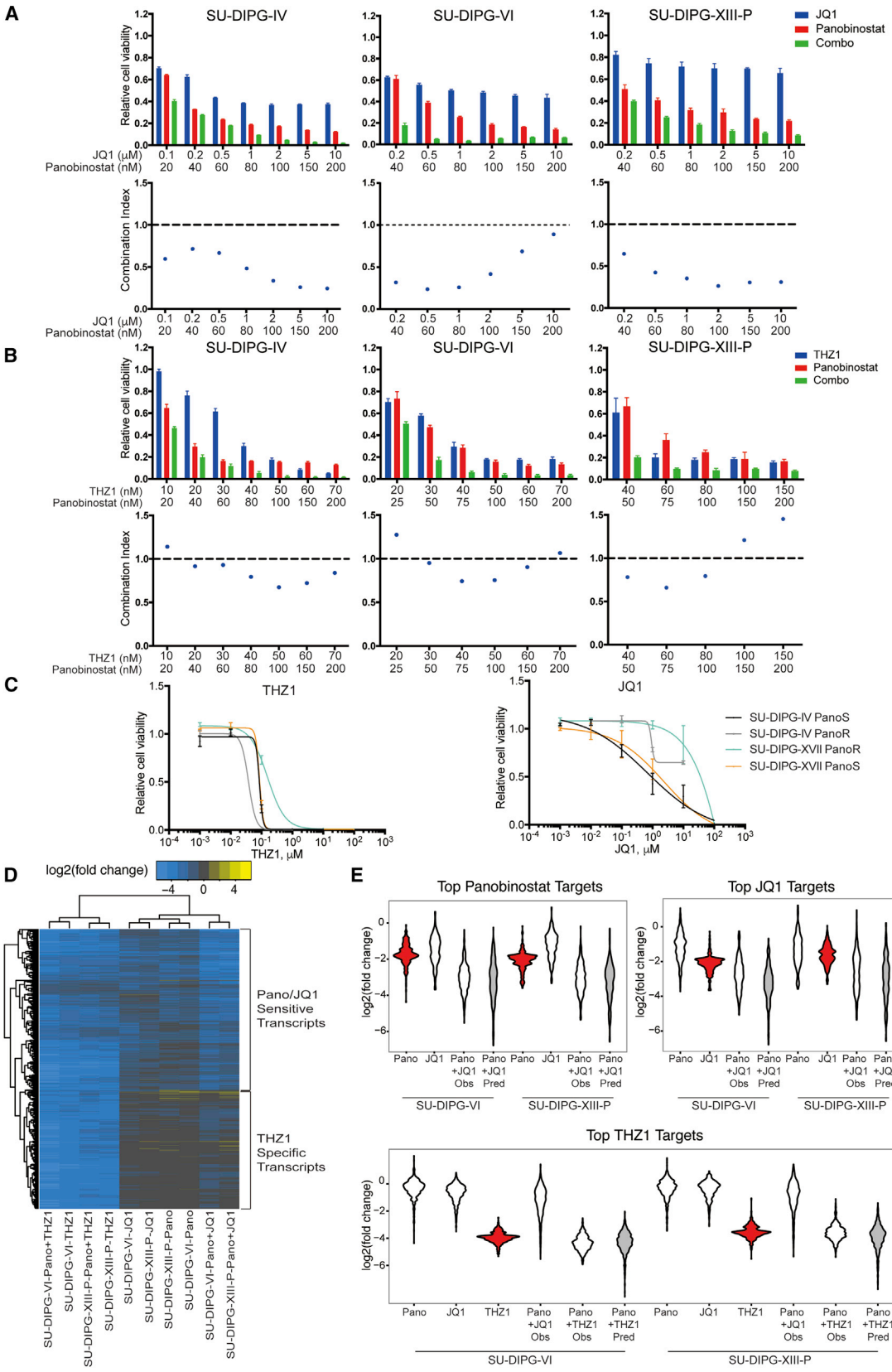

(legend on next page)

exhibit resistance to JQ1 (Figure 3C). This shared resistance suggests similar mechanisms of disrupting cellular viability between panobinostat and JQ1.

To better understand the interaction of these therapies, we characterized the genes disrupted by panobinostat, JQ1, and THZ1. We performed RNA sequencing (RNA-seq) after 24 hr of treatment with panobinostat, THZ1, or JQ1 alone or in combination. As in other malignant models (Chipumuro et al., 2014; Christensen et al., 2014; Kwiatkowski et al., 2014), we observed global downregulation of active transcripts with THZ1 treatment (Figure S3F) and downregulation of specific subsets of genes by JQ1 (Figure S3F; Delmore et al., 2011; Dawson et al., 2011).

We then examined the top target genes of panobinostat, JQ1, and THZ1. Unsupervised hierarchical clustering revealed that panobinostat and JQ1 caused similar transcriptional changes, downregulating many of the same genes and clustering apart from cells treated with THZ1 (Figures 3D and 3E), thus explaining the shared resistance described above. By contrast, the top targets of THZ1 showed very little disruption with panobinostat or JQ1. Combinatorial treatment of panobinostat with JQ1 or THZ1 resulted in the greatest downregulation of each of these genes, with changes consistent with an additive effect of single-agent treatments. Thus, panobinostat and JQ1 may synergistically disrupt cell viability by creating stronger inhibition at a common set of genes than either single treatment. In contrast, panobinostat and THZ1 preferentially disrupt distinct sets of genes and may achieve synergy by disrupting a larger number of genes in combination than in single treatment.

To further understand the mechanisms mediating cell viability disruption, we performed gene ontology analysis on the top downregulated target genes of each drug (Figure S3G). THZ1-treated cells showed preferential disruption of genes related to transcription and gene regulation, such as *ETS1*, *ELF4*, *MGA*, *SOX10*, and *HES5*. In contrast, both JQ1 and panobinostat disrupted key regulators of nervous system development, including *NTRK3*, *LINGO1*, *ASCL1*, *SYT4*, *SYT17*, *MYT1*, *MYRF*, and *SALL3*. In addition, both drugs disrupted genes that enriched for synapse organization and structure, with one panobinostat target being *NLGN3*, a key mechanism mediating neuronal activity-regulated glioma growth (Venkatesh et al., 2015).

Together, these data show that targeting RNAPII-dependent transcription in conjunction with HDAC inhibition is more effective than either drug alone. Panobinostat-resistant cells retain sensitivity to THZ1, suggesting that CDK7 blockade together with HDAC inhibition may be a promising combination strategy for DIPG.

Identification of Super-enhancers in DIPG Reveals Potential Therapeutic Targets and Cell-Identity Genes

CDK7 and bromodomain inhibition both preferentially disrupt transcription at genes associated with super-enhancers (Lovén et al., 2013; Chipumuro et al., 2014; Christensen et al., 2014; Jiang et al., 2016). Super-enhancers (SEs) are large clusters of enhancer elements displaying unusually high levels of activating marks, such as H3K27 acetylation (H3K27Ac), and transcription complex subunit binding, including RNAPII and BRD4 (Whyte et al., 2013). The genes associated with SEs in cancer are enriched for drivers of oncogenic state as well as normal regulators of cell identity (Lovén et al., 2013; Hnisz et al., 2013). Given the effectiveness of these therapies in inhibiting DIPG growth, we characterized the SE landscape of DIPG through H3K27Ac chromatin immunoprecipitation followed by high-throughput sequencing (ChIP-seq) in three DIPG H3.3K27M cultures (SU-DIPG-VI, SU-DIPG-XIII-P, and SU-DIPG-XVII) and one H3.1K27M mutant (SU-DIPG-IV) culture, and annotated each SE with its nearest transcription start site (TSS) (Figures 4A and 4B; for full list see Table S4). A number of the genes associated with SEs were markers of undifferentiated neural cell state, including *SOX2* and *NES*. Many were genes of oligodendroglial lineage identity, including genes classically associated with oligodendrocyte precursor cells such as *SOX10*, *CSPG4* (also known as *NG2*), *NKX2.2*, *PDGFRA*, *OLIG2*, and *LINGO1*, as well as genes expressed by oligodendroglial lineage cells during differentiation such as *OLIG1*, *MYRF*, *MYT1*, and *MBP*. These findings lend support to the notion that DIPG may originate from a precursor cell early in differentiation in the oligodendroglial lineage (Monje et al., 2011; Tate et al., 2015).

To identify commonalities in DIPG biology, we considered shared SEs between four cultures, defined as overlapping SEs present in at least three of the cultures studied. When linked to gene expression levels quantified by RNA-seq (Figure 4C), we observed that the genes associated with these shared SEs represent a set of transcripts highly expressed in both culture and in previously published primary tissue, likely identifying a core set of genes controlling both DIPG cell identity and malignant state. We then performed an analysis using the Genomic Regions Enrichment of Annotations Tool (GREAT) (McLean et al., 2010) on all shared SE regions (Figure 4D) and observed enrichment for regulators of CNS differentiation and neurogenesis, as well as genes controlling axon guidance and neuron projection morphogenesis.

Regulators of signal transduction were also heavily enriched. As SEs in malignant cells often mark key pathways maintaining

Figure 3. JQ1 and THZ1 Synergize with HDACi against DIPG

(A and B) Viability and synergy in combinatorial drug treatments. DIPG cultures treated with JQ1 (A) or THZ1 (B) and panobinostat individually or in combination at indicated concentrations for 72 hr (top). Cell viabilities were measured and normalized to 0.1% DMSO control values (n = 3 wells per data point). (Bottom) Combination index value (CI) of each drug combination condition was calculated by using CalcuSyn software. A CI of less than 1 indicated synergy between two drugs.

(C) Panobinostat-resistant cells (PanoR) were generated by chronic treatment at IC_{50} concentration for 21 days. Cells were treated as indicated for 3 days and normalized to DMSO control (n = 3 wells per data point).

(D) Log_2(fold change) over DMSO control of the top 10% of panobinostat and JQ1 downregulated genes and top 5% of THZ1 downregulated genes active in both cultures. Cells were treated with panobinostat (100 nM), JQ1 (1 μM), and THZ1 (100 nM) for 24 hr.

(E) Violin plots showing log_2(fold change) of the top 10% downregulated panobinostat and JQ1 targets and top 5% downregulated THZ1 targets. Gray plots indicate the predicted log_2(fold change) assuming an additive interaction of single treatments. Red plots highlight the response of the top target genes of each category in single treatment.

Data are shown as mean ± SD unless otherwise indicated. See also Figure S3.

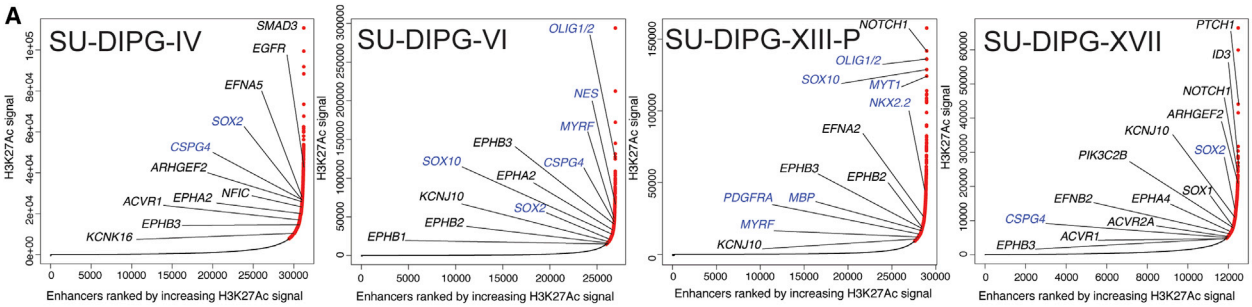

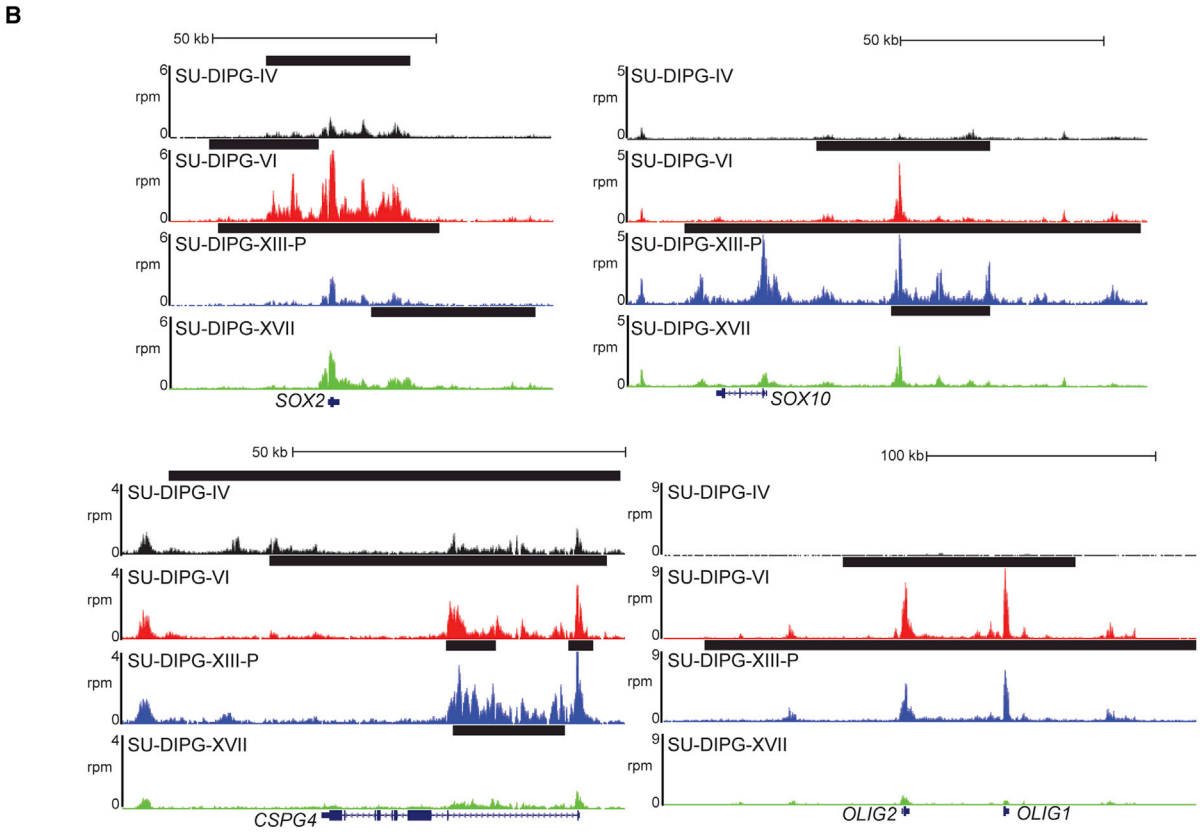

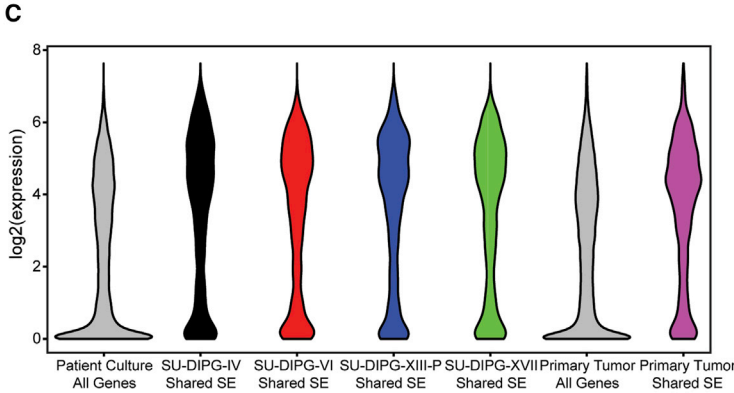

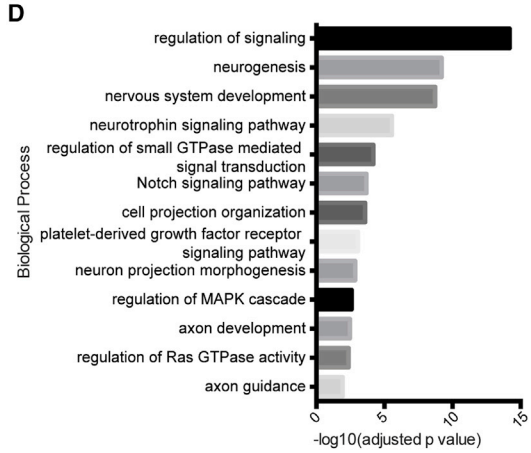

(legend on next page)

oncogenic state, we examined the pathways associated with these genes using PANTHER analysis (Mi et al., 2016; Figure 5A). This may represent a key list for developing targeted therapy in DIPG. Consistent with this notion, we observed enrichment for a number of pathways previously described as dysregulated and important to DIPG biology, including NOTCH (Taylor et al., 2015), Hedgehog (Monje et al., 2011), and PDGF (platelet-derived growth factor) (Paugh et al., 2013). These signaling pathways enriched for common downstream kinases (*MAPK1*, *MAPK3K1*, *MAP3K2*, *MAPK8*, *MAPK11*, *MAPAPK2*, *PRKCA*, *PRKCD*, *PRKCE*, and *PRKCZ*). As EGF (epidermal growth factor), FGF (fibroblast growth factor), Ras, Hedgehog, and others of these signaling pathways converge upon MAPK/ERK and mTOR signaling (Cristea and Sage, 2016; Switon et al., 2017; Kim et al., 2016; McCubrey et al., 2016), we hypothesized that targeting these downstream pathways may be an effective way to simultaneously disrupt multiple oncogenic pathways. Cell viability was disrupted in two out of four cell cultures when treated with ERK1/2 inhibitor SCH772984 (Morris et al., 2013) and all four cell cultures with dual mTORC1/2 inhibitor AZD8055 (Chresta et al., 2010) at submicromolar concentrations (AZD8055: median IC_{50} 0.12 μM; Figure 5B).

We found a large number of potassium (K^+) channel genes associated with SEs in DIPG (Figure 5C). Preclinical work in lung and breast cancers (Sun et al., 2016), as well as medulloblastoma (Huang et al., 2015), has shown targeting of K^+ channels to be therapeutically effective. As we observed a large number K^+ channels across a variety of channel families (voltage-gated, inward-rectifying, two-pore, Ca^{2+}-activated) to be expressed in DIPG, we targeted all K^+ channels using 10 mM cesium chloride (CsCl). CsCl specifically blocks the pores of K^+ channels and is an agent standardly used in electrophysiology for specific K^+ channel blockade without acute toxicity to normal brain tissue (Walz et al., 2002). When compared with equimolar sodium chloride, controlling for changes in chloride content and overall osmolarity, we found that 10 mM CsCl reduced DIPG cell viability in all four DIPG cell cultures tested (Figures 5D and S4A). Interestingly, many K^+ channel genes exhibited strong downregulation with all three transcriptional therapies (Figure S4B), potentially accounting for part of the disruption of cell viability that these drugs display. As K^+ channels play roles in regulating membrane voltage and cell size changes during the cell cycle (Huang and Jan 2014), we hypothesized that their blockade may disrupt the ability of DIPG cells to progress through the cell cycle. After 10 hr of CsCl treatment, we did not observe a difference in the number of dead cells (Figures S4C–S4E) but rather a significant increase in the fraction of DIPG cells in G_2/M with a decrease in the fraction of cells in S phase in two of the cultures tested (Figure 5E). Considering that we observed a decrease in viability in all four cultures tested, we believe that disruption of cell-cycle progression accounts only for part of the mechanism of K^+ channel blockade vulnerability in DIPG. Taken together, these data indicate that targeting K^+ channels disrupts DIPG cell growth and underscore K^+ channels as a target in DIPG.

EPH Receptor Signaling Plays a Role in DIPG Cell Migration and Invasion

GREAT analysis of shared SEs exhibited enrichment for genes controlling neuron projection and axon guidance (Figure 4D). A number of ephrin and EPH receptors were associated with SEs in all four patient-derived cell cultures (Figure 6A). EPH-ephrin signaling classically plays a role in axon pathfinding during normal neurodevelopment (Cramer and Miko, 2016; Hruska and Dalva, 2012; Xu and Henkemeyer, 2012) and represents a promising target in a number of CNS malignancies including medulloblastoma, ependymoma, and adult glioblastoma (Bhatia et al., 2015; Chen et al., 2015; Miao et al., 2015; Nakada et al., 2004, 2006). To study the role of EPH-ephrin signaling in DIPG, we used LDN-211904 (Qiao et al., 2009), a selective inhibitor of forward EPH receptor signaling. Treatment with LDN-211904 did not substantially inhibit cell viability at concentrations less than 10 μM (Figure S5A), but 5 μM LDN-211904 drastically reduced cell invasion in all four DIPG cell cultures tested (Figures 6B and S5B). Furthermore, EPH blockade resulted in a dramatic, dose-dependent reduction in both SU-DIPG-XVII invasion (Figure 6C) and SU-DIPG-IV migration (Figure 6D) in a 3D Matrigel spheroid assay (Vinci et al., 2013, 2015). Many of the EPH receptors and ephrins expressed by SU-DIPG-VI and SU-DIPG-XIII-P did not show downregulation with panobinostat or JQ1 (Figure S5C). This suggests that additional therapy beyond HDAC or bromodomain inhibition would be needed to clinically target the effect of these signaling molecules on DIPG invasion.

Overall, we show here that blockade of EPH receptor signaling significantly reduces DIPG cell migration and invasion in vitro. EPH-ephrin signaling may represent an important pathogenic mechanism facilitating the diffuse and invasive spread of DIPG throughout the brainstem and, in most cases of DIPG, throughout much of the brain (Caretti et al., 2014).

Panobinostat and THZ1 Disrupt Super-enhancer Biology

We found the set of SE-associated genes in SU-DIPG-VI and SU-DIPG-XIII-P to be enriched in the set of downregulated targets of both JQ1 and THZ1 (Figures S6A and S6B), consistent with previous findings (Christensen et al., 2014; Chipumuro et al., 2014; Lovén et al., 2013), as well as panobinostat. As panobinostat increases H3K27me3 levels (Grasso et al., 2015), we hypothesized that panobinostat may disrupt the H3K27Ac

Figure 4. Identification of Super-enhancers in DIPG

(A) Enhancers ranked by H3K27Ac signal over input. SEs are marked in red and regular enhancers are indicated in black. Genes in blue represent genes informative toward cell identity.

(B) ChIP-seq profiles for SE-associated genes. The x axis represents genomic position and the y axis represents normalized reads per million (rpm). Black bars represent SE calls.

(C) Expression of shared SE-associated genes. Log_2-transformed expression values for each cell culture were plotted for all genes or the nearest RefSeq gene to each shared SE. Primary tumor values represent analysis of previously published data (Grasso et al., 2015).

(D) Gene ontology biological processes associated with shared SE-associated genes identified by GREAT analysis with binomial false discovery rate (FDR) adjusted p values reported. See also Table S4.

A

Pathway	Genes
Hedgehog signaling pathway	*PTCH1, GLI2, GLI3, CSNK1E, SUFU, GSK3B*
EGF receptor signaling pathway	*EGF, EGFR, PRKCA, PRKCD, PRKCE, PRKCZ, RASA2, MAPK1, MAP3K1, MAP3K2, MAPK8, MAPK11, YWHAG, YWHAZ, SPRY2, SPRY4, PLCG1, DAB2IP*
p38 MAPK pathway	*MEF2C, MEF2A, DUSP10, DUSP1, MAPKAPK2, MAPK11, HSPB1*
TGF-beta signaling pathway	*SMAD3, SMAD4, SMAD7, INHBB, BMP7, BMP8A, TGFBR1, SKI, MAPK1, MAPK8, MAPK11, JUN*
Ras Pathway	*RALGDS, GSK3A, GSK3B, RHOB, MAPK1, MAPK8, MAP3K1, MAPKAPK2, MAPK11, JUN, TIAM1*
PDGF signaling pathway	*PDGFRA, PDGFRB, PDGFB, ARHGAP12, ARHGAP26, MYC, GSK3A, GSK3B, JUN, PRKCA, RASA2, RHOB, PLCG1, VAV2, MAPK1, MAPK8, MAP3K2, MAPAPK2*
Ionotropic glutamate receptor pathway	*GRIK1, GRIK3, CACNA1A, CACNA1E, CACNG5, CAMK2B, VAMP3, SLC13*
FGF signaling pathway	*FGF1, FGFR1, RASA2, SPRY2, SPRY4, PLCG1, PRKCA, PRKCD, PRKCE, PRKCZ, YWHAG, YWHAZ, MAPK1, MAPK8, MAPK11, MAP3K1, MAP3K2*
Notch signaling pathway	*NOTCH1, JAG1, LFNG, NEURL1, DLK1, RBPJ*
Integrin signalling pathway	*ITGB1, ASAP1, RAPGEF1, CSK, PTK2, FYN, RHOB, MAPK1, MAP3K1, MAP3K2, MAPK8, ARF6, ARHGAP26*
VEGF signaling pathway	*VEGFA, PRKCA, PRKCD, PRKCE, PRKCZ, PTK2, PLCG1, MAPK1, MAPKAPK2, HSPB1*

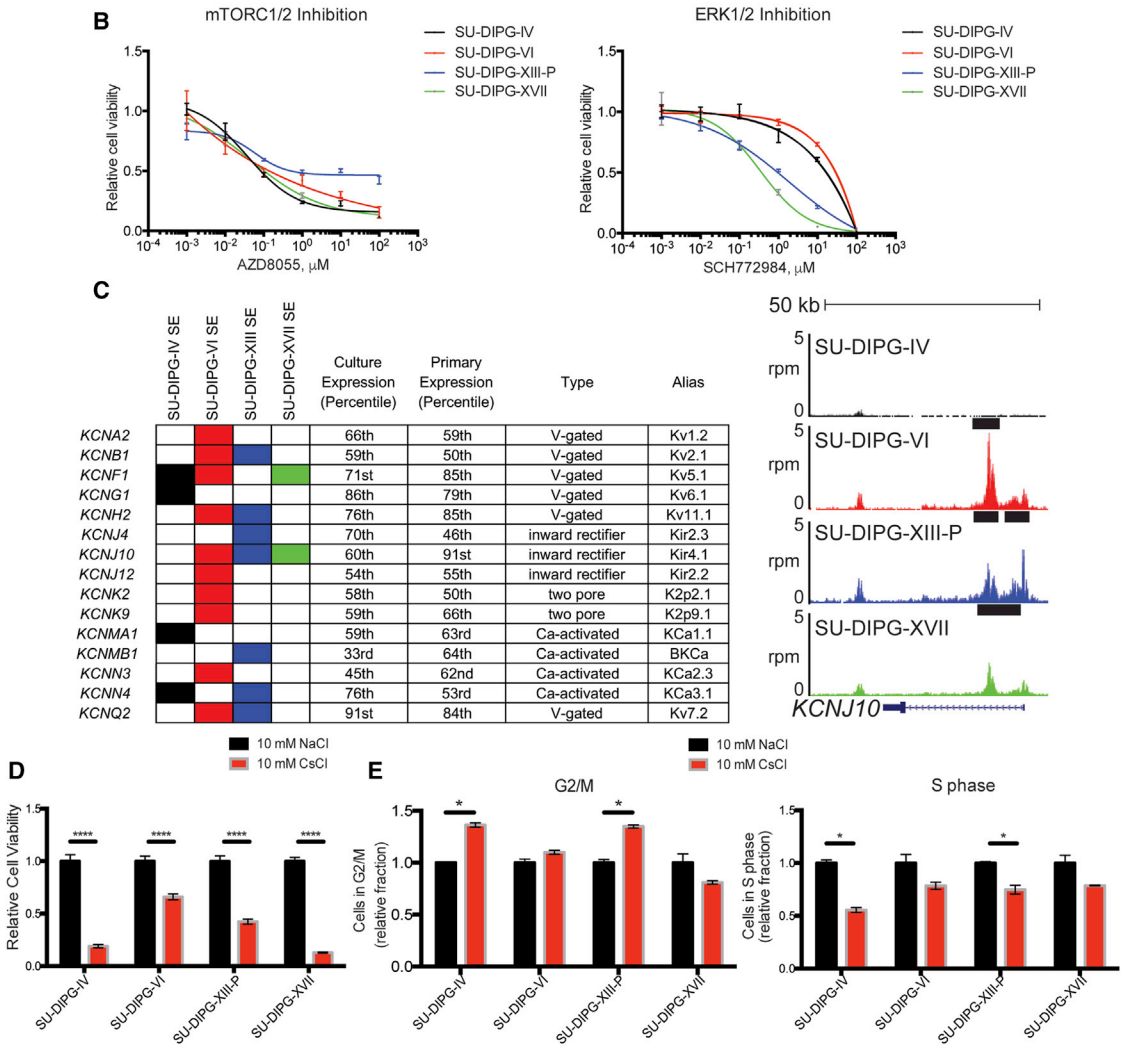

Figure 5. Super-enhancers Reveal Gene Families Essential to DIPG Cell Viability

(A) Table of select pathways enriched in SE-associated genes. Enriched pathways identified by PANTHER pathway analysis of genes in the "signal transduction" term from Figure 4D.

(B) Cultures were treated with AZD8055 or SCH772984 as indicated for 72 hr. Cell viabilities were normalized to 1% DMSO control values. Data are shown as mean ± SD (n = 3 or 4 wells per data point).

(legend continued on next page)

mark at SEs. Consistent with this notion, H3K27Ac ChIP-seq following 24 hr of panobinostat treatment resulted in reduced enrichment of H3K27Ac at SEs (Figures 7A and 7B). When examining all H3K27Ac peaks, we observed that panobinostat reduced H3K27Ac density selectively at the strongest regions in control cells (Figure 7C), with most peaks showing little change. The genes associated with these regions showed enrichment for the top panobinostat target genes (Figures S6C and S6D), consistent with the proposed mechanism of panobinostat. When we examined the distance of these panobinostat target genes from the nearest TSS, we saw a large proportion of the sites located distal to any TSS (Figure 7D), suggesting that panobinostat disrupts H3K27Ac at both enhancer and promoter regions.

Finally, to identify core regulators of DIPG malignant state, we looked for SE-associated genes strongly disrupted in both SU-DIPG-VI and SU-DIPG-XIII-P with panobinostat (at least 2-fold) or THZ1 treatment (at least 8-fold; Figures 7E and S6E). Forty-eight shared panobinostat targets were associated with an SE in both SU-DIPG-VI and SU-DIPG-XIII-P and 41 shared THZ1-sensitive genes were linked to SEs in both cell cultures (Table S5). We believe these sets of genes to be fundamental to DIPG biology. Intriguingly, these gene sets also contained a number of genes involved in axonal guidance (*NAV1*, *SEMA4C*; Maes et al., 2002; Martínez-López et al., 2005; Maier et al., 2011), neurite outgrowth (*NINJ1*; Araki et al., 1997; Araki and Milbrandt, 1996), synapse formation (*LRFN4*; Mah et al., 2010), and glutamate receptor function (*CNIH3*, *GRIK3*; Herring et al., 2013; Strutz et al., 2001; Figure S6F). These genes classically associated with neuronal communication suggest that DIPG cell interaction with neurons in the tumor microenvironment may be central to DIPG biology, reinforcing the notion that disruption of neuron-glioma interactions represents a prime target for therapeutic development (Venkatesh et al., 2015).

DISCUSSION

No progress has been made in extending life for children with DIPG since the introduction of radiotherapy nearly four decades ago. However, a surge in DIPG research in recent years may prove to turn the tide. Comprehensive genomic studies identified the oncohistone H3K27M as the hallmark of pediatric gliomas affecting the midline of the CNS (Wu et al., 2012; Schwartzentruber et al., 2012; Khuong-Quang et al., 2012; Gessi et al., 2015; Shankar et al., 2016). Central to DIPG oncogenesis (Funato et al., 2014), the presence of H3K27M mutant histones alters the function of the PRC2 complex responsible for H3K27 trimethylation (Lewis et al., 2013) and results in broad dysregulation of transcription (Chan et al., 2013). The creation of patient-derived DIPG cell culture and orthotopic xenograft models has allowed for preclinical drug testing studies, revealing epigenetic therapies, such as histone demethylase inhibition (Hashizume et al., 2014) and HDAC inhibition with panobinostat (Grasso et al., 2015) as promising therapeutic strategies. Panobinostat was subsequently taken to phase I trial for children with DIPG (NCT02717455). While panobinostat may ultimately prove to be of clinical utility, it was clear from the preclinical studies that the best hope for this agent would be a temporary reprieve from tumor growth (Grasso et al., 2015; Hennika et al., 2017), as resistance to mono-agent therapy does develop (Grasso et al., 2015). The present study represents an effort to identify a combination strategy focused on complementary modulation of H3K27M-related transcriptional aberrations that would extend and improve upon the efficacy of panobinostat alone.

The data presented here demonstrate that DIPG is vulnerable to disruption of transcription both in vitro and in vivo. As previously shown, transcriptional inhibition mediated by JQ1 bromodomain inhibition impedes DIPG cell viability in vitro (Taylor et al., 2015). We expand upon this finding by examining a range of bromodomain inhibitors and by demonstrating BRD4 as the key target using shRNA-mediated BRD4 knockdown. Our findings are consistent with a predicted role for BRD4 in H3K27M transcriptional pathology, based on the observation that Brd1 and Brd4 are associated with H3K27M-containing nucleosomes in a *Drosophila* model of H3K27M expression (Herz et al., 2014). While more potent bromodomain inhibitor compounds exhibiting better brain penetration are needed for clinical translation of these findings, bromodomain inhibition may be an effective clinical therapy when the appropriate drugs are available. However, it is important to note that bromodomain inhibition appears cytostatic rather than cytocidal and that DIPG cells resistant to HDAC inhibition also exhibit concomitant resistance to bromodomain inhibition.

Disruption of transcription through CDK7 inhibition using THZ1 also impairs DIPG cell viability. The effect of CDK7 inhibition is cytocidal, and THZ1 therapy results in a modest increase in survival in a patient-derived DIPG xenograft model. However, CDK7 inhibitors with better brain penetration are needed for optimal clinical translation. Transcriptional inhibition via either BRD4 or CDK7 blockade shows therapeutic synergy with HDAC inhibition using panobinostat, and panobinostat-resistant DIPG cells retain vulnerability to THZ1. Thus, a combination strategy may prove to be of clinical utility when brain-penetrant transcriptional inhibitor compounds are available for clinical use or with alternative delivery strategies such as direct intratumoral infusion using convection-enhanced delivery.

Transcriptomic analyses following treatment with single and combinatorial panobinostat, JQ1, and THZ1 therapy provided insights as to how these epigenetic modifying agents disrupt gene expression. SE-associated genes were preferentially disrupted

(C) Filled-in rectangles represent association with an SE in the indicated cell culture. Expression percentiles shown for mean expression value in either the four cell cultures indicated or SU-DIPG primary tumor samples published in Grasso et al. (2015). For genome tracks shown, the x axis represents genomic position and y axis shows normalized reads per million (rpm). Black bars represent SE calls.

(D) Patient-derived DIPG cultures were treated with 10 mM cesium chloride or sodium chloride for 3 days. Cell viabilities were normalized to NaCl controls; ****$p < 0.001$ for all data shown.

(E) FACS cell-cycle analysis of DIPG cultures treated with 10 mM NaCl or CsCl for 10 hr before addition of EdU for 1 hr. Data are shown as proportion of cells in G_2/M normalized to NaCl control. *Adjusted $p < 0.05$.

Data in (D) and (E) are presented as mean ± SEM (n = 3). Student's t test was performed with Holm-Sidak correction. See also Figure S4.

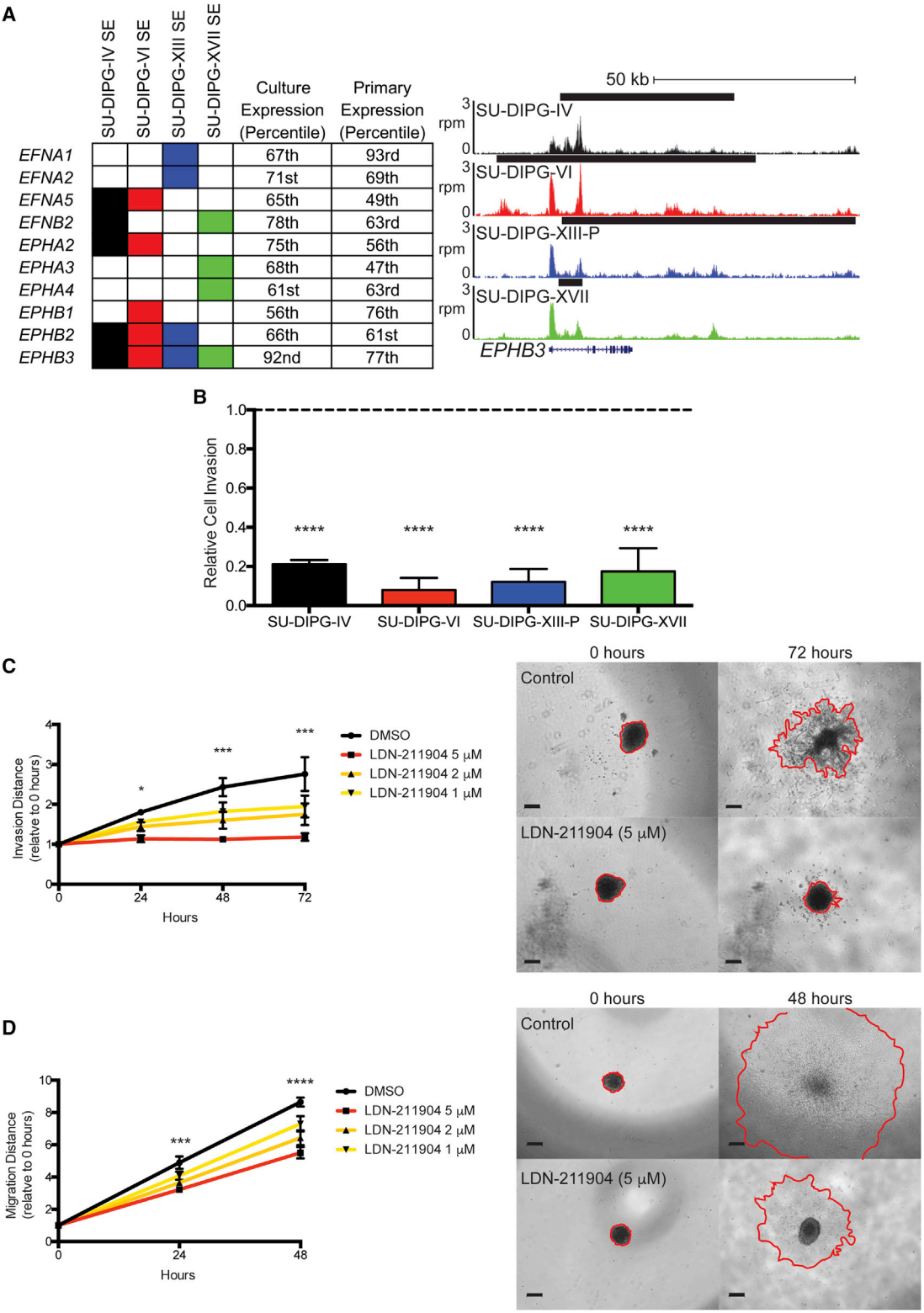

Figure 6. EPH Signaling Is Important to DIPG Invasion

(A) EPH receptors and ephrins associated with an SE in DIPG. Filled-in rectangles represent association with an SE in the indicated cell culture. Expression percentiles shown for mean expression value in either the four cell cultures indicated or SU-DIPG primary tumor samples published in Grasso et al. (2015). For genome tracks shown, the x axis represents genomic position and y axis shows normalized reads per million (rpm). Black bars represent SE calls.

(legend continued on next page)

by all three therapies, and the H3K27Ac mark was lost at SEs following panobinostat treatment. We found that the top targets JQ1 and panobinostat were similar, potentially explaining our finding that panobinostat-resistant cells also display functional resistance to JQ1. By contrast, the set of genes identified as the top targets of THZ1 is only mildly inhibited by panobinostat or JQ1 treatment. As BRD family proteins couple activating histone marks to transcription (Wu and Chiang, 2007; LeRoy et al., 2008; Rahman et al., 2011), we hypothesize that JQ1 and panobinostat may synergistically inhibit DIPG viability through orthogonal disruption of a common set of core genes, with JQ1 disrupting BRD4 activity at active histone marks and panobinostat restoring K27me3 at the same set of marks. By contrast, the set of genes disproportionately downregulated by THZ1 treatment are largely non-overlapping with the targets of panobinostat, and synergy may be achieved in combinatorial treatment by disrupting a larger overall number of genes than in single therapy.

To elucidate the chromatin landscape of DIPG, we performed ChIP-seq analyses of four patient-derived cell cultures. As nearly 80% of DIPG patients exhibit the K27M mutation in H3.3 or H3.1 (Khuong-Quang et al., 2012; Schwartzentruber et al., 2012; Wu et al., 2012), which has been shown to cause global histone hypomethylation (Bender et al., 2013; Lewis et al., 2013), the location of activating histone marks such as H3K27Ac may reveal genes that fail to undergo suppression during development and lead to tumor formation. Identification of SEs in DIPG provides insights into the genes maintaining the malignant state of DIPG as well as insights regarding the cell of origin. These analyses revealed a large number of oligodendroglial lineage genes associated with SEs in DIPG, including *PDGFRA*, *OLIG1*, *OLIG2*, *NKX2.2*, *CSPG4*, and *SOX10* among others, as well as several genes marking an early neural precursor state, such as *SOX2* and *NES*, supporting a leading hypothesis that the cell of origin of DIPG may be an early oligodendrocyte precursor cell (Monje et al., 2011; Tate et al., 2015).

The SE analyses highlighted numerous genes classically involved in neurodevelopment or neuronal communication, underscoring the recently demonstrated importance of neuron-glioma interactions (Venkatesh et al., 2015) and the emerging concept that pediatric gliomas hijack and recapitulate mechanisms of development. Prominent were axon pathfinding genes, such as a number of EPH receptors and ephrins. Functional analyses demonstrated that this canonical axon pathfinding pathway plays a robust role in DIPG cell migration and invasion. These findings are consistent with the invasion-promoting role of the EPH-ephrin pathway in adult gliobastoma (Nakada et al., 2004, 2006; Miao et al., 2015). We also found a large number of K^+ channel genes associated with SEs and demonstrated that, like several other cancers (Sun et al., 2016), DIPG cells are vulnerable to K^+ channel blockade. These genomic findings provide a deeper understanding of DIPG pathobiology and elucidate potential targets for DIPG therapy. Although the number of potential targets dysregulated in DIPG suggests that epigenetic therapies that simultaneously disrupt aberrant expression of numerous target genes may be required as a part of any effective therapeutic strategy, some of the genes identified as upregulated and functionally important, such as EPH-ephrins, were not downregulated by the transcriptional inhibitors studied here and may require targeted therapy.

In summary, the data presented here demonstrate that disruption of transcription is a promising therapeutic strategy for DIPG when drugs with sufficient brain penetration are developed, particularly when administered together with an HDAC inhibitor. DIPG SE analyses support the hypothesis that the cell of origin for DIPG is a precursor cell in the oligodendroglial lineage and uncover several vulnerabilities of DIPG, elucidating fundamental pathological mechanisms promoting DIPG growth and invasion.

STAR★METHODS

Detailed methods are provided in the online version of this paper and include the following:

- KEY RESOURCES TABLE
- CONTACT FOR REAGENT AND RESOURCE SHARING
- EXPERIMENTAL MODEL AND SUBJECT DETAILS
  - Patient-Derived DIPG Cell Cultures
  - DIPG Orthotopic Xenograft Model and Drug Testing
- METHOD DETAILS
  - Cell Viability and Combinatorial Drug Synergy
  - Proliferation, Apoptosis, and Cell Cycle Assays
  - Lentivirus Preparation and Infection
  - Western Blotting
  - LC-MS/MS Analysis of Tissue and Serum Concentration
  - ChIP and Library Preparation
  - RNA Sequencing
  - Boyden Chamber Invasion Assays
  - 3D Migration and Invasion Assays
- QUANTIFICATION AND STATISTICAL ANALYSIS
  - Statistical Analyses
  - ChIP-seq Analyses
  - Gene Expression Analyses
  - 3D Migration and Invasion Quantification
- DATA AND SOFTWARE AVAILABILITY
- ADDITIONAL RESOURCES

(B) Transwell Matrigel invasion following treatment with LDN-211904 (5 μM). Invading cell quantification was normalized to mean DMSO invasion. ****p Values versus DMSO: SU-DIPG-IV p = 0.0006, SU-DIPG-VI p = 0.0003, SU-DIPG-XIII-P p = 0.0004, SU-DIPG-XVII p = 0.0004.

(C) (Left) Quantification of invasion distance of SU-DIPG-XVII cells treated with LDN-211904 at the concentrations indicated or DMSO control. Invasion distance normalized to day-0 distance for each sphere. p values of DMSO versus 5 μM LDN-211904: 24 hr, *p = 0.0311; 48 hr, ***p = 0.0005; 72 hr, ***p = 0.0001. (Right) Representative images of spheroid invasion at 0 and 72 hr, with leading edge outlined in red. Scale bars, 200 μm.

(D) (Left) Quantification of migration distance of SU-DIPG-IV cells treated with LDN-211904 at the concentrations indicated or DMSO control. Migration distance normalized to day-0 distance for each sphere. Student's two-tailed t test (FDR = 0.05) between DMSO and 5 μM LDN-211904. FDR adjusted p values: ***p = 0.0004, ****p < 0.0001. (Right) Representative images of spheroid migration at 0 and 48 hr, with leading edge outlined in red. Scale bars, 200 μm.

Data are shown as mean ± SEM (n = 3); Student's t test with Holm-Sidak adjustment unless otherwise indicated. See also Figure S5.

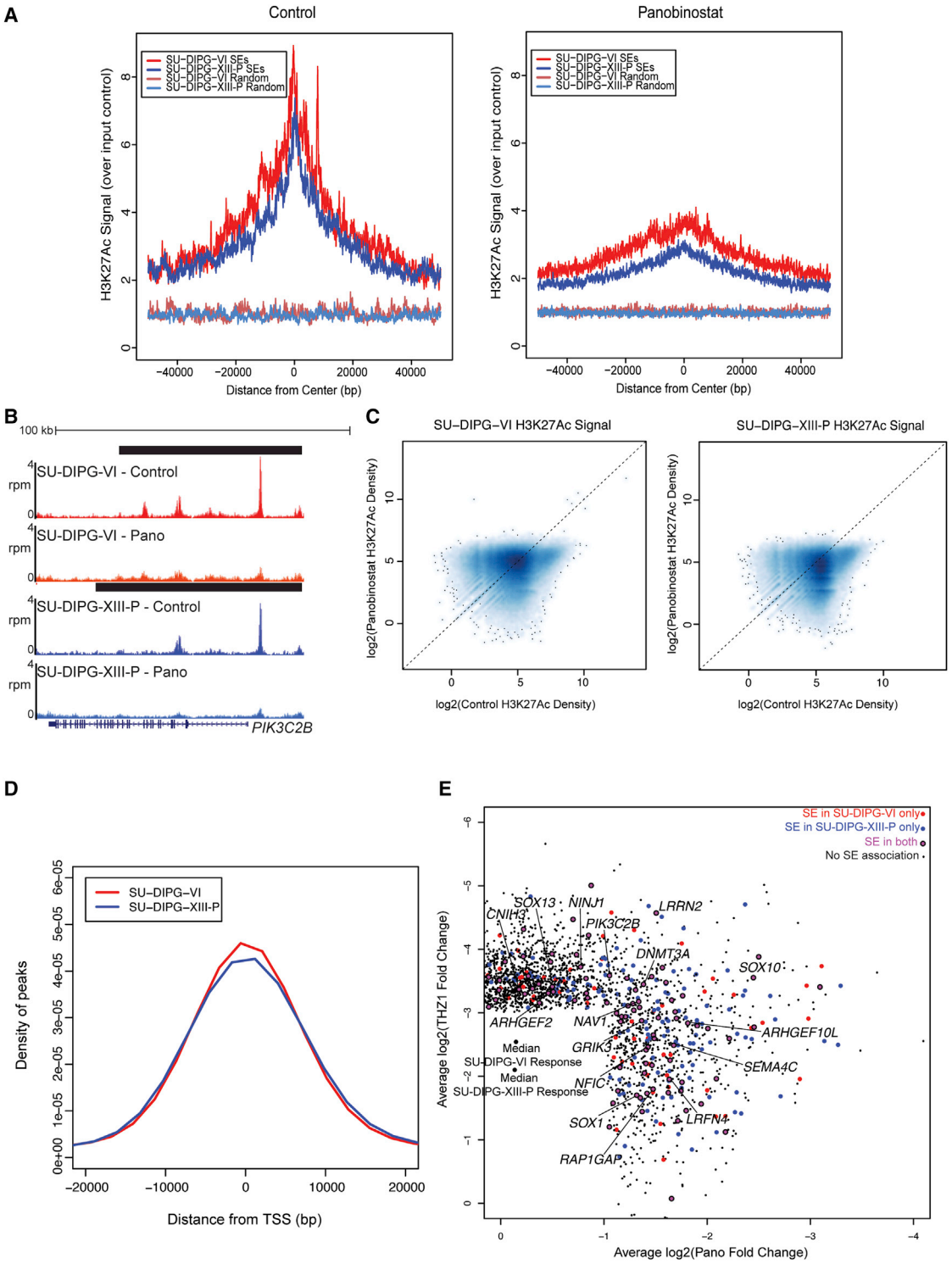

Figure 7. Disruption of Super-enhancers with Panobinostat and THZ1

(A) SU-DIPG-VI or SU-DIPG-XIII-P cultures treated with panobinostat for 24 hr. H3K27Ac ChIP-seq enrichment over input was plotted for all SEs or an equivalent number of randomly generated regions of median length.

(B) Representative example of H3K27Ac at an SE before and after panobinostat administration; x axis represents genomic position and y axis shows normalized reads per million (rpm). Black bars represent SE calls.

(C) Log_2-transformed H3K27Ac signal density plotted for all peaks identified. Dashed line marks equivalent signal in both DMSO control and panobinostat treated samples. Higher density of points is indicated by darker shading.

(legend continued on next page)

SUPPLEMENTAL INFORMATION

Supplemental Information includes six figures and five tables and can be found with this article online at http://dx.doi.org/10.1016/j.ccell.2017.03.011.

AUTHOR CONTRIBUTIONS

S.N., Y.T., N.A.V., and K.R.T. conducted experiments and contributed to experimental design, manuscript editing, and data analysis. P.W. contributed to conducting in vivo experiments. W.S. conducted liquid chromatography-tandem mass spectrometry analyses. A.P. designed and validated the shRNA constructs. F.L., W.M., M.L., L.Z., and J.M. contributed to the in vitro experiments. E.H. generated the H3WT DIPG cell culture. T.S. and J.W. contributed to the genomics analyses. Y.T. and S.N. made the figures. M.M., N.A.V. and S.N. wrote the manuscript. M.M. and Y.T. supervised all aspects of the work.

ACKNOWLEDGMENTS

We thank Rintaro Hashizume and C. David James for use of the SF7761 cell line, and Eric Raabe for use of the JHH-DIPG1 cell line. The authors gratefully acknowledge support from McKenna Claire Foundation (M.M.), Lyla Nsouli Foundation (M.M.), Alex's Lemonade Stand Foundation (M.M. and Y.T.), The Cure Starts Now Foundation and DIPG Collaborative (M.M.), Unravel Pediatric Cancer (M.M.), National Institute of Neurological Disorders and Stroke (R01NS092597 to M.M.), Department of Defense (NF140075 to M.M.), California Institute for Regenerative Medicine (CIRM RN3-06510 to M.M.), Childhood Brain Tumor Foundation (M.M.), V Foundation (M.M.), Joey Fabus Childhood Cancer Foundation (M.M.), Wayland Villars DIPG Foundation (M.M.), Connor Johnson, Zoey Ganesh, Abigail Jensen and Declan Gloster Memorial Funds (M.M.), N8 Foundation (M.M.), Godfrey Family Fund in Memory of Fiona Penelope (M.M.), Virginia and D.K. Ludwig Fund for Cancer Research (M.M.), Child Health Research Institute at Stanford Anne T. and Robert M. Bass Endowed Faculty Scholarship in Pediatric Cancer (M.M.), Liwei Wang Research Fund (M.M.), The Recruitment Program of Global Experts of China (National 1000-Youth Talents Program; Y.T.), The Program for Professor of Special Appointment (Eastern Scholar) at Shanghai Institutions of Higher Learning (Y.T.), National Natural Science Foundation of China (81572761 to Y.T.), Shanghai Rising-Star Program (Y.T.), Howard Hughes Medical Institute (NIH R01 GM112720-01 to J.W.) and March of Dimes Foundation (J.W.).

Received: August 29, 2016
Revised: December 27, 2016
Accepted: March 22, 2017
Published: April 20, 2017

REFERENCES

Araki, T., and Milbrandt, J. (1996). Ninjurin, a novel adhesion molecule, is induced by nerve injury and promotes axonal growth. Neuron *17*, 353–361.

Araki, T., Zimonjic, D.B., Popescu, N.C., and Milbrandt, J. (1997). Mechanism of homophilic binding mediated by ninjurin, a novel widely expressed adhesion molecule. J. Biol. Chem. *272*, 21373–21380.

Ashburner, M., Ball, C.A., Blake, J.A., Botstein, D., Butler, H., Cherry, J.M., Davis, A.P., Dolinski, K., Dwight, S.S., Eppig, J.T., et al. (2000). Gene ontology: tool for the unification of biology. Nat. Genet. *25*, 25–29.

Bender, S., Tang, Y., Lindroth, A.M., Hovestadt, V., Jones, D.T., Kool, M., Zapatka, M., Northcott, P.A., Sturm, D., Wang, W., et al. (2013). Reduced H3K27me3 and DNA hypomethylation are major drivers of gene expression in K27M mutant pediatric high-grade gliomas. Cancer Cell *24*, 660–672.

Bhatia, S., Hirsch, K., Baig, N.A., Rodriguez, O., Timofeeva, O., Kavanagh, K., Lee, Y.C., Wang, X.J., Albanese, C., and Karam, S.D. (2015). Effects of altered ephrin-A5 and EphA4/EphA7 expression on tumor growth in a medulloblastoma mouse model. J. Hematol. Oncol. *8*, 105.

Bid, H.K., Phelps, D.A., Xaio, L., Guttridge, D.C., Lin, J., London, C., Baker, L.H., Mo, X., and Houghton, P.J. (2016). The bromodomain bet inhibitor jq1 suppresses tumor angiogenesis in models of childhood sarcoma. Mol. Cancer Ther. *15*, 1018–1028.

Brown, Z.Z., Müller, M.M., Jain, S.U., Allis, C.D., Lewis, P.W., and Muir, T.W. (2014). Strategy for "detoxification" of a cancer-derived histone mutant based on mapping its interaction with the methyltransferase PRC2. J. Am. Chem. Soc. *136*, 13498–13501.

Buczkowicz, P., Hoeman, C., Rakopoulos, P., Pajovic, S., Letourneau, L., Dzamba, M., Morrison, A., Lewis, P., Bouffet, E., Bartels, U., et al. (2014). Genomic analysis of diffuse intrinsic pontine gliomas identifies three molecular subgroups and recurrent activating ACVR1 mutations. Nat. Genet. *46*, 451–456.

Caretti, V., Bugiani, M., Freret, M., Schellen, P., Jansen, M., van Vuurden, D., Kaspers, G., Fisher, P.G., Hulleman, E., Wesseling, P., et al. (2014). Subventricular spread of diffuse intrinsic pontine glioma. Acta Neuropathol. *128*, 605–607.

Chan, K.-M., Fang, D., Gan, H., Hashizume, R., Yu, C., Schroeder, M., Gupta, N., Mueller, S., James, C.D., Jenkins, R., et al. (2013). The histone H3.3K27M mutation in pediatric glioma reprograms H3K27 methylation and gene expression. Genes Dev. *27*, 985–990.

Chen, P., Rossi, N., Priddy, S., Pierson, C.R., Studebaker, A.W., and Johnson, R.A. (2015). EphB2 activation is required for ependymoma development as well as inhibits differentiation and promotes proliferation of the transformed cell. Sci. Rep. *5*, 9248.

Chipumuro, E., Marco, E., Christensen, C.L., Kwiatkowski, N., Zhang, T., Hatheway, C.M., Abraham, B.J., Sharma, B., Yeung, C., Altabef, A., et al. (2014). CDK7 Inhibition suppresses super-enhancer-linked oncogenic transcription in MYCN-driven cancer. Cell *159*, 1126–1139.

Chresta, C.M., Davies, B.R., Hickson, I., Harding, T., Cosulich, S., Critchlow, S.E., Vincent, J.P., Ellston, R., Jones, D., Sini, P., et al. (2010). AZD8055 is a potent, selective, and orally bioavailable ATP-competitive mammalian target of rapamycin kinase inhibitor with in vitro and in vivo antitumor activity. Cancer Res. *70*, 288–298.

Christensen, C.L., Kwiatkowski, N., Abraham, B.J., Carretero, J., Al-Shahrour, F., Zhang, T., Chipumuro, E., Herter-Sprie, G.S., Akbay, E.A., Altabef, A., et al. (2014). Targeting transcriptional addictions in small cell lung cancer with a covalent CDK7 inhibitor. Cancer Cell *26*, 909–922.

Coudé, M.-M., Braun, T., Berrou, J., Dupont, M., Bertrand, S., Masse, A., Raffoux, E., Itzykson, R., Delord, M., Riveiro, M.E., et al. (2015). BET inhibitor OTX015 targets BRD2 and BRD4 and decreases c-MYC in acute leukemia cells. Oncotarget *6*, 17698–17712.

Cramer, K.S., and Miko, I.J. (2016). Eph-ephrin signaling in nervous system development. F1000Res. *5*, 413.

Cristea, S., and Sage, J. (2016). Is the canonical RAF/MEK/ERK signaling pathway a therapeutic target in SCLC? J. Thorac. Oncol. *11*, 1233–1241.

Dawson, M.A., Prinjha, R.K., Dittmann, A., Giotopoulos, G., Bantscheff, M., Chan, W.I., Robson, S.C., Chung, C.W., Hopf, C., Savitski, M.M., et al.

(D) Distance was calculated between differential H3K27Ac peaks with the strongest levels of H3K27Ac density in control treated cells and the nearest TSS. The x axis represents distance from the closest TSS in base pairs and the y axis represents probability density.
(E) Top targets in DIPG. Scatter of active transcripts showing greater than 2-fold reduction with panobinostat and greater than 8-fold reduction with THZ1 treatment in both cultures. Plotted values are the mean $\log_2$(fold change) between SU-DIPG-VI and SU-DIPG-XIII-P. Transcripts shown in magenta are associated with an SE in both cell cultures, those shown in red are associated with an SE in SU-DIPG-VI only, and those shown in blue are associated with an SE in SU-DIPG-XIII-P only. Black points are transcripts with no SE association.
See also Figure S6 and Table S5.

(2011). Inhibition of BET recruitment to chromatin as an effective treatment for MLL-fusion leukaemia. Nature *478*, 529–533.

Delmore, J.E., Issa, G.C., Lemieux, M.E., Rahl, P.B., Shi, J., Jacobs, H.M., Kastritis, E., Gilpatrick, T., Paranal, R.M., Qi, J., et al. (2011). BET bromodomain inhibition as a therapeutic strategy to target c-Myc. Cell *146*, 904–917.

Filippakopoulos, P., and Knapp, S. (2014). Targeting bromodomains: epigenetic readers of lysine acetylation. Nat. Rev. Drug Discov. *13*, 337–356.

Fisher, R.P., and Morgan, D.O. (1994). A novel cyclin associates with M015/CDK7 to form the CDK-activating kinase. Cell *78*, 713–724.

Funato, K., Major, T., Lewis, P.W., Allis, C.D., and Tabar, V. (2014). Use of human embryonic stem cells to model pediatric gliomas with H3.3K27M histone mutation. Science *346*, 1529–1533.

Gessi, M., Gielen, G.H., Dreschmann, V., Waha, A., and Pietsch, T. (2015). High frequency of H3F3A K27M mutations characterizes pediatric and adult high-grade gliomas of the spinal cord. Acta Neuropathol. *130*, 435–437.

Glover-Cutter, K., Larochelle, S., Erickson, B., Zhang, C., Shokat, K., Fisher, R.P., and Bentley, D.L. (2009). TFIIH-associated Cdk7 kinase functions in phosphorylation of C-terminal domain Ser7 residues, promoter-proximal pausing, and termination by RNA polymerase II. Mol. Cell Biol. *29*, 5455–5464.

Grasso, C.S., Tang, Y., Truffaux, N., Berlow, N.E., Liu, L., Debily, M.A., Quist, M.J., Davis, L.E., Huang, E.C., Woo, P.J., et al. (2015). Functionally defined therapeutic targets in diffuse intrinsic pontine glioma. Nat. Med. *21*, 555–559.

Hagenbuchner, J., and Ausserlechner, M.J. (2016). Targeting transcription factors by small compounds—current strategies and future implications. Biochem. Pharmacol. *107*, 1–13.

Hashizume, R., Smirnov, I., Liu, S., Phillips, J.J., Hyer, J., McKnight, T.R., Wendland, M., Prados, M., Banerjee, A., Nicolaides, T., et al. (2012). Characterization of a diffuse intrinsic pontine glioma cell line: implications for future investigations and treatment. J. Neurooncol. *110*, 305–313.

Hashizume, R., Andor, N., Ihara, Y., Lerner, R., Gan, H., Chen, X., Fang, D., Huang, X., Tom, M.W., Ngo, V., et al. (2014). Pharmacologic inhibition of histone demethylation as a therapy for pediatric brainstem glioma. Nat. Med. *20*, 1394–1396.

Heinz, S., Benner, C., Spann, N., Bertolino, E., Lin, Y.C., Laslo, P., Cheng, J.X., Murre, C., Singh, H., and Glass, C.K. (2010). Simple combinations of lineage-determining transcription factors prime cis-regulatory elements required for macrophage and B cell identities. Mol. Cell *38*, 576–589.

Hennika, T., Hu, G., Olaciregui, N.G., Barton, K.L., Ehteda, A., Chitranjan, A., Chang, C., Gifford, A.J., Tsoli, M., Ziegler, D.S., et al. (2017). Pre-clinical study of panobinostat in xenograft and genetically engineered murine diffuse intrinsic pontine glioma models. PLoS One *12*, e0169485.

Herring, B.E., Shi, Y., Suh, Y.H., Zheng, C.Y., Blankenship, S.M., Roche, K.W., and Nicoll, R.A. (2013). Cornichon proteins determine the subunit composition of synaptic AMPA receptors. Neuron *77*, 1083–1096.

Herz, H.M., Morgan, M., Gao, X., Jackson, J., Rickels, R., Swanson, S.K., Florens, L., Washburn, M.P., Eissenberg, J.C., and Shilatifard, A. (2014). Histone H3 lysine-to-methionine mutants as a paradigm to study chromatin signaling. Science *345*, 1065–1070.

Hnisz, D., Abraham, B.J., Lee, T.I., Lau, A., Saint-André, V., Sigova, A.A., Hoke, H.A., and Young, R.A. (2013). Super-enhancers in the control of cell identity and disease. Cell *155*, 934–947.

Hruska, M., and Dalva, M.B. (2012). Ephrin regulation of synapse formation, function and plasticity. Mol. Cell Neurosci. *50*, 35–44.

Huang, X., and Jan, L.Y. (2014). Targeting potassium channels in cancer. J. Cell Biol. *206*, 151–162.

Huang, X., He, Y., Dubuc, A.M., Hashizume, R., Zhang, W., Reimand, J., Yang, H., Wang, T.A., Stehbens, S.J., Younger, S., et al. (2015). EAG2 potassium channel with evolutionarily conserved function as a brain tumor target. Nat. Neurosci. *18*, 1236–1246.

Jang, M.K., Mochizuki, K., Zhou, M., Jeong, H.S., Brady, J.N., and Ozato, K. (2005). The bromodomain protein Brd4 is a positive regulatory component of P-TEFb and stimulates RNA polymerase II-dependent transcription. Mol. Cell *19*, 523–534.

Jiang, Y.Y., Lin, D.C., Mayakonda, A., Hazawa, M., Ding, L.W., Chien, W.W., Xu, L., Chen, Y., Xiao, J.F., Senapedis, W., et al. (2016). Targeting super-enhancer-associated oncogenes in oesophageal squamous cell carcinoma. Gut. http://dx.doi.org/10.1136/gutjnl-2016-311818.

Khuong-Quang, D.A., Buczkowicz, P., Rakopoulos, P., Liu, X.Y., Fontebasso, A.M., Bouffet, E., Bartels, U., Albrecht, S., Schwartzentruber, J., Letourneau, L., et al. (2012). K27M mutation in histone H3.3 defines clinically and biologically distinct subgroups of pediatric diffuse intrinsic pontine gliomas. Acta Neuropathol. *124*, 439–447.

Kim, D., Pertea, G., Trapnell, C., Pimentel, H., Kelley, R., and Salzberg, S.L. (2013). TopHat2: accurate alignment of transcriptomes in the presence of insertions, deletions and gene fusions. Genome Biol. *14*, R36.

Kim, L.C., Cook, R.S., and Chen, J. (2016). mTORC1 and mTORC2 in cancer and the tumor microenvironment. Oncogene. http://dx.doi.org/10.1038/onc.2016.363.

Kwiatkowski, N., Zhang, T., Rahl, P.B., Abraham, B.J., Reddy, J., Ficarro, S.B., Dastur, A., Amzallag, A., Ramaswamy, S., Tesar, B., et al. (2014). Targeting transcription regulation in cancer with a covalent CDK7 inhibitor. Nature *511*, 616–620.

Langmead, B., and Salzberg, S.L. (2012). Fast gapped-read alignment with Bowtie 2. Nat. Methods *9*, 357–359.

Larochelle, S., Merrick, K.A., Terret, M.E., Wohlbold, L., Barboza, N.M., Zhang, C., Shokat, K.M., Jallepalli, P.V., and Fisher, R.P. (2007). Requirements for Cdk7 in the assembly of Cdk1/cyclin B and activation of Cdk2 revealed by chemical genetics in human cells. Mol. Cell *25*, 839–850.

Larochelle, S., Amat, R., Glover-Cutter, K., Sansó, M., Zhang, C., Allen, J.J., Shokat, K.M., Bentley, D.L., and Fisher, R.P. (2012). Cyclin-dependent kinase control of the initiation-to-elongation switch of RNA polymerase II. Nat. Struct. Mol. Biol. *19*, 1108–1115.

LeRoy, G., Rickards, B., and Flint, S.J. (2008). The double bromodomain proteins Brd2 and Brd3 couple histone acetylation to transcription. Mol. Cell *30*, 51–60.

Lewis, P.W., Müller, M.M., Koletsky, M.S., Cordero, F., Lin, S., Banaszynski, L.A., Garcia, B.A., Muir, T.W., Becher, O.J., and Allis, C.D. (2013). Inhibition of PRC2 activity by a gain-of-function H3 mutation found in pediatric glioblastoma. Science *340*, 857–861.

Liao, Y., Smyth, G.K., and Shi, W. (2014). featureCounts: an efficient general purpose program for assigning sequence reads to genomic features. Bioinformatics *30*, 923–930.

Love, M.I., Huber, W., and Anders, S. (2014). Moderated estimation of fold change and dispersion for RNA-seq data with DESeq2. Genome Biol. *15*, 550.

Lovén, J., Hoke, H.A., Lin, C.Y., Lau, A., Orlando, D.A., Vakoc, C.R., Bradner, J.E., Lee, T.I., and Young, R.A. (2013). Selective inhibition of tumor oncogenes by disruption of super-enhancers. Cell *153*, 320–334.

Maes, T., Barceló, A., and Buesa, C. (2002). Neuron navigator: a human gene family with homology to unc-53, a cell guidance gene from *Caenorhabditis elegans*. Genomics *80*, 21–30.

Mah, W., Ko, J., Nam, J., Han, K., Chung, W.S., and Kim, E. (2010). Selected SALM (synaptic adhesion-like molecule) family proteins regulate synapse formation. J.Neurosci. *30*, 5559–5568.

Maier, V., Jolicoeur, C., Rayburn, H., Takegahara, N., Kumanogoh, A., Kikutani, H., Tessier-Lavigne, M., Wurst, W., and Friedel, R.H. (2011). Semaphorin 4C and 4G are ligands of Plexin-B2 required in cerebellar development. Mol. Cell Neurosci. *46*, 419–431.

Martínez-López, M.J., Alcántara, S., Mascaró, C., Pérez-Brangulí, F., Ruiz-Lozano, P., Maes, T., Soriano, E., and Buesa, C. (2005). Mouse Neuron navigator 1, a novel microtubule-associated protein involved in neuronal migration. Mol. Cell Neurosci. *28*, 599–612.

McCubrey, J.A., Rakus, D., Gizak, A., Steelman, L.S., Abrams, S.L., Lertpiriyapong, K., Fitzgerald, T.L., Yang, L.V., Montalto, G., Cervello, M., et al. (2016). Effects of mutations in Wnt/β-catenin, hedgehog, Notch and PI3K pathways on GSK-3 activity—diverse effects on cell growth, metabolism and cancer. Biochim. Biophys. Acta *1863*, 2942–2976.

McLean, C.Y., Bristor, D., Hiller, M., Clarke, S.L., Schaar, B.T., Lowe, C.B., Wenger, A.M., and Bejerano, G. (2010). GREAT improves functional interpretation of cis-regulatory regions. Nat. Biotechnol. *28*, 495–501.

Mertz, J.A., Conery, A.R., Bryant, B.M., Sandy, P., Balasubramanian, S., Mele, D.A., Bergeron, L., and Sims, R.J. (2011). Targeting MYC dependence in cancer by inhibiting BET bromodomains. Proc. Natl. Acad. Sci. USA *108*, 16669–16674.

Mi, H., Poudel, S., Muruganujan, A., Casagrande, J.T., and Thomas, P.D. (2016). PANTHER version 10: expanded protein families and functions, and analysis tools. Nucleic Acids Res. *44*, D336–D342.

Miao, H., Gale, N.W., Guo, H., Qian, J., Petty, A., Kaspar, J., Murphy, A.J., Valenzuela, D.M., Yancopoulos, G., Hambardzumyan, D., et al. (2015). EphA2 promotes infiltrative invasion of glioma stem cells in vivo through cross-talk with Akt and regulates stem cell properties. Oncogene *34*, 558–567.

Mirguet, O., Gosmini, R., Toum, J., Clément, C.A., Barnathan, M., Brusq, J.M., Mordaunt, J.E., Grimes, R.M., Crowe, M., Pineau, O., et al. (2013). Discovery of epigenetic regulator I-BET762: lead optimization to afford a clinical candidate inhibitor of the BET bromodomains. J. Med. Chem. *56*, 7501–7515.

Monje, M., Mitra, S.S., Freret, M.E., Raveh, T.B., Kim, J., Masek, M., Attema, J.L., Li, G., Haddix, T., Edwards, M.S., et al. (2011). Hedgehog-responsive candidate cell of origin for diffuse intrinsic pontine glioma. Proc. Natl. Acad. Sci. USA *108*, 4453–4458.

Morris, E.J., Jha, S., Restaino, C.R., Dayananth, P., Zhu, H., Cooper, A., Carr, D., Deng, Y., Jin, W., Black, S., et al. (2013). Discovery of a novel ERK inhibitor with activity in models of acquired resistance to BRAF and MEK inhibitors. Cancer Discov. *3*, 742–750.

Nakada, M., Drake, K.L., Nakada, S., Niska, J.A., and Berens, M.E. (2006). Ephrin-B3 ligand promotes glioma invasion through activation of Rac1. Cancer Res. *66*, 8492–8500.

Nakada, M., Niska, J.A., Miyamori, H., McDonough, W.S., Wu, J., Sato, H., and Berens, M.E. (2004). The phosphorylation of EphB2 receptor regulates migration and invasion of human glioma cells. Cancer Res. *64* (9), 3179–3185.

Ostrom, Q.T., Gittleman, H., Fulop, J., Liu, M., Blanda, R., Kromer, C., Wolinsky, Y., Kruchko, C., and Barnholtz-Sloan, J.S. (2015). CBTRUS statistical report: primary brain and central nervous system tumors diagnosed in the United States in 2008-2012. Neuro Oncol. *17* (*Suppl 4*), iv1–iv62.

Paugh, B.S., Zhu, X., Qu, C., Endersby, R., Diaz, A.K., Zhang, J., Bax, D.A., Carvalho, D., Reis, R.M., Onar-Thomas, A., et al. (2013). Novel oncogenic PDGFRA mutations in pediatric high-grade gliomas. Cancer Res. *73* (20), 6219–6229.

Picaud, S., Fedorov, O., Thanasopoulou, A., Leonards, K., Jones, K., Meier, J., Olzscha, H., Monteiro, O., Martin, S., Philpott, M., et al. (2015). Generation of a selective small molecule inhibitor of the CBP/p300 bromodomain for leukemia therapy. Cancer Res. *75*, 5106–5119.

Posternak, V., and Cole, M.D. (2016). Strategically targeting MYC in cancer. F1000Res. *5*, http://dx.doi.org/10.12688/f1000research.7879.1.

Qiao, L., Choi, S., Case, A., Gainer, T.G., Seyb, K., Glicksman, M.A., Lo, D.C., Stein, R.L., and Cuny, G.D. (2009). Structure-activity relationship study of EphB3 receptor tyrosine kinase inhibitors. Bioorg. Med. Chem. Lett. *19* (21), 6122–6126.

Quinlan, A.R., and Hall, I.M. (2010). BEDTools: a flexible suite of utilities for comparing genomic features. Bioinformatics *26*, 841–842.

Rahman, S., Sowa, M.E., Ottinger, M., Smith, J.A., Shi, Y., Harper, J.W., and Howley, P.M. (2011). The Brd4 extraterminal domain confers transcription activation independent of pTEFb by recruiting multiple proteins, including NSD3. Mol. Cell Biol. *31*, 2641–2652.

Rossignol, M., Kolb-Cheynel, I., and Egly, J.M. (1997). Substrate specificity of the cdk-activating kinase (CAK) is altered upon association with TFIIH. EMBO J. *16*, 1628–1637.

Schwartzentruber, J., Korshunov, A., Liu, X.Y., Jones, D.T., Pfaff, E., Jacob, K., Sturm, D., Fontebasso, A.M., Quang, D.A., Tönjes, M., et al. (2012). Driver mutations in histone H3.3 and chromatin remodelling genes in paediatric glioblastoma. Nature *482*, 226–231.

Sengupta, D., Kannan, A., Kern, M., Moreno, M.A., Vural, E., Stack, B., Jr., Suen, J.Y., Tackett, A.J., and Gao, L. (2015a). Disruption of BRD4 at H3K27Ac-enriched enhancer region correlates with decreased c-Myc expression in Merkel cell carcinoma. Epigenetics *10*, 460–466.

Sengupta, S., Biarnes, M.C., Clarke, R., and Jordan, V.C. (2015b). Inhibition of BET proteins impairs estrogen-mediated growth and transcription in breast cancers by pausing RNA polymerase advancement. Breast Cancer Res. Treat. *150*, 265–278.

Serizawa, H., Mäkelä, T.P., Conaway, J.W., Conaway, R.C., Weinberg, R.A., and Young, R.A. (1995). Association of Cdk-activating kinase subunits with transcription factor TFIIH. Nature *374*, 280–282.

Shahbazi, J., Liu, P.Y., Atmadibrata, B., Bradner, J.E., Marshall, G.M., Lock, R.B., and Liu, T. (2016). The bromodomain inhibitor JQ1 and the histone deacetylase inhibitor panobinostat synergistically reduce N-Myc expression and induce anticancer effects. Clin. Cancer Res. *22*, 2534–2544.

Shankar, G.M., Lelic, N., Gill, C.M., Thorner, A.R., Van Hummelen, P., Wisoff, J.H., Loeffler, J.S., Brastianos, P.K., Shin, J.H., Borges, L.F., et al. (2016). BRAF alteration status and the histone H3F3A gene K27M mutation segregate spinal cord astrocytoma histology. Acta Neuropathol. *131*, 147–150.

Strutz, N., Villmann, C., Thalhammer, A., Kizelsztein, P., Eisenstein, M., Teichberg, V.I., and Hollmann, M. (2001). Identification of domains and amino acids involved in GLuR7 ion channel function. J. Neurosci. *21*, 401–411.

Subramanian, A., Tamayo, P., Mootha, V.K., Mukherjee, S., Ebert, B.L., Gillette, M.A., Paulovich, A., Pomeroy, S.L., Golub, T.R., Lander, E.S., and Mesirov, J.P. (2005). Gene set enrichment analysis: a knowledge-based approach for interpreting genome-wide expression profiles. Proc. Natl. Acad. Sci. USA *102*, 15545–15550.

Sun, H., Luo, L., Lal, B., Ma, X., Chen, L., Hann, C.L., Fulton, A.M., Leahy, D.J., Laterra, J., and Li, M. (2016). A monoclonal antibody against KCNK9 K+ channel extracellular domain inhibits tumour growth and metastasis. Nat. Commun. *7*, 10339.

Switon, K., Kotulska, K., Janusz-Kaminska, A., Zmorzynska, J., and Jaworski, J. (2017). Molecular neurobiology of mTOR. Neuroscience *341*, 112–153.

Tang, Y., Gholamin, S., Schubert, S., Willardson, M.I., Lee, A., Bandopadhayay, P., Bergthold, G., Masoud, S., Nguyen, B., Vue, N., et al. (2014). Epigenetic targeting of Hedgehog pathway transcriptional output through BET bromodomain inhibition. Nat. Med. *20*, 732–740.

Tate, M.C., Lindquist, R.A., Nguyen, T., Sanai, N., Barkovich, A.J., Huang, E.J., Rowitch, D.H., and Alvarez-Buylla, A. (2015). Postnatal growth of the human pons: a morphometric and immunohistochemical analysis. J. Comp. Neurol. *523*, 449–462.

Taylor, K.R., Mackay, A., Truffaux, N., Butterfield, Y.S., Morozova, O., Philippe, C., Castel, D., Grasso, C.S., Vinci, M., Carvalho, D., et al. (2014). Recurrent activating ACVR1 mutations in diffuse intrinsic pontine glioma. Nat. Genet. *46*, 457–461.

Taylor, I.C., Hütt-Cabezas, M., Brandt, W.D., Kambhampati, M., Nazarian, J., Chang, H.T., Warren, K.E., Eberhart, C.G., and Raabe, E.H. (2015). Disrupting NOTCH slows diffuse intrinsic pontine glioma growth, enhances radiation sensitivity, and shows combinatorial efficacy with bromodomain inhibition. J. Neuropathol. Exp. Neurol. *74*, 778–790.

Venkatesh, H.S., Johung, T.B., Caretti, V., Noll, A., Tang, Y., Nagaraja, S., Gibson, E.M., Mount, C.W., Polepalli, J., Mitra, S.S., et al. (2015). Neuronal activity promotes glioma growth through neuroligin-3 secretion. Cell *161*, 803–816.

Venneti, S., Garimella, M.T., Sullivan, L.M., Martinez, D., Huse, J.T., Heguy, A., Santi, M., Thompson, C.B., and Judkins, A.R. (2013). Evaluation of histone 3 lysine 27 trimethylation (H3K27me3) and enhancer of Zest 2 (EZH2) in pediatric glial and glioneuronal tumors shows decreased H3K27me3 in H3F3A K27M mutant glioblastomas. Brain Pathol. *23*, 558–564.

Vinci, M., Box, C., Zimmermann, M., and Eccles, S.A. (2013). Tumor spheroid-based migration assays for evaluation of therapeutic agents. Methods Mol. Biol. *986*, 253–266.

Vinci, M., Box, C., and Eccles, S.A. (2015). Three-dimensional (3D) tumor spheroid invasion assay. J. Vis. Exp. e52686, http://dx.doi.org/10.3791/52686.

Walz, W., Boulton, A.A., Alan, A., and Baker, G.B. (2002). Patch-Clamp Analysis: Advanced Techniques (Humana Press).

Wang, Y., Zhang, T., Kwiatkowski, N., Abraham, B.J., Lee, T.I., Xie, S., Yuzugullu, H., Von, T., Li, H., Lin, Z., et al. (2015). CDK7-dependent transcriptional addiction in triple-negative breast cancer. Cell *163*, 174–186.

Whyte, W.A., Orlando, D.A., Hnisz, D., Abraham, B.J., Lin, C.Y., Kagey, M.H., Rahl, P.B., Lee, T.I., and Young, R.A. (2013). Master transcription factors and mediator establish super-enhancers at key cell identity genes. Cell *153*, 307–319.

Wu, S.-Y., and Chiang, C.-M. (2007). The double bromodomain-containing chromatin adaptor Brd4 and transcriptional regulation. J. Biol. Chem. *282*, 13141–13145.

Wu, G., Broniscer, A., McEachron, T.A., Lu, C., Paugh, B.S., Becksfort, J., Qu, C., Ding, L., Huether, R., Parker, M., et al.; St. Jude Children's Research Hospital–Washington University Pediatric Cancer Genome Project (2012). Somatic histone H3 alterations in pediatric diffuse intrinsic pontine gliomas and non-brainstem glioblastomas. Nat. Genet. *44*, 251–253.

Xu, N.-J., and Henkemeyer, M. (2012). Ephrin reverse signaling in axon guidance and synaptogenesis. Semin. Cell Dev. Biol. *23*, 58–64.

Zhang, Z., Ma, P., Jing, Y., Yan, Y., Cai, M.C., Zhang, M., Zhang, S., Peng, H., Ji, Z.L., Di, W., et al. (2016). BET bromodomain inhibition as a therapeutic strategy in ovarian cancer by downregulating FoxM1. Theranostics *6*, 219–230.

Zuber, J., Shi, J., Wang, E., Rappaport, A.R., Herrmann, H., Sison, E.A., Magoon, D., Qi, J., Blatt, K., Wunderlich, M., et al. (2011). RNAi screen identifies Brd4 as a therapeutic target in acute myeloid leukaemia. Nature *478*, 524–528.

STAR★METHODS

KEY RESOURCES TABLE

REAGENT or RESOURCE	SOURCE	IDENTIFIER
Antibodies		
Rabbit polyclonal anti-RNAPII	Santa Cruz Biotechnology	Cat# sc-899; RRID: AB_632359
Rabbit polyclonal anti-RNAPII-CTD-SER2	Bethyl	Cat# A300-654A-M; RRID: AB_519341
Rabbit polyclonal anti-RNAPII-CTD-SER5	Bethyl	Cat# A304-408A-M; RRID: AB_2620602
Rabbit monoclonal anti-RNAPII-CTD-SER7	Cell Signaling	Cat# 13780S
Rabbit polyclonal anti-CDK7	Bethyl	Cat# A300-405A; RRID: AB_2275973
Rabbit monoclonal anti-beta Actin	Cell Signaling	Cat# 4970S; RRID: AB_2223172
Rabbit polyclonal anti-BRD4	Bethyl	Cat# A301-985A100; RRID: AB_2620184
Rabbit polyclonal anti-beta Tubulin	Abcam	Cat# ab6046; RRID: AB_2210370
Rabbit polyclonal anti-H3K27Ac	Active Motif	Cat# 39133; RRID: AB_2561016
Chemicals, Peptides, and Recombinant Proteins		
JQ1	Selleckchem	Cat# S7110
Panobinostat	Selleckchem	Cat# S1030
OTX015	Selleckchem	Cat# S7360
iBET762	Selleckchem	Cat# S7189
AZD8055	Selleckchem	Cat# S1555
SCH772984	Selleckchem	Cat# S7101
THZ1	Millipore	Cat# 532372
LDN-211904	Millipore	Cat# 428201
Critical Commercial Assays		
Celltiter Glo	Promega	Cat# G7571
Alexa Fluor 488 or 647 Flow Cytometry Assay Kit	Invitrogen	Cat# C10420, C10419
Annexin V-FITC Apoptosis Detection Kit II	BD Biosicences	Cat# 556570
NEBNext Illumina Multiplex Oligo Adaptors	New England Biolabs	Cat# E7335S
ERCC Spike-In Controls	Thermo	Cat# 4456740
Dynabeads mRNA Purification Kit	Ambion	Cat# 61006
Biocoat Matrigel Invasion Chambers	Corning	Cat# 354480
Matrigel Basement Membrane Matrix, LDEV-Free	Corning	Cat# 354234
Deposited Data		
Raw and processed data	This paper	GEO: GSE94259
Human reference genome hg19, GRCh37	Genome Reference Consortium	http://www.ncbi.nlm.nih.gov/projects/genome/assembly/grc/human/
RefSeq Gene Annotations	UCSC Genome Browser	https://genome.ucsc.edu/
Experimental Models: Cell Lines		
Human: Patient-derived DIPG cell cultures	This paper	Tables S1 and S2
Experimental Models: Organisms/Strains		
Mouse: NOD-SCID-IL2 gamma chain-deficient	Jackson Laboratory	Stock No. 005557
Recombinant DNA		
Human BRD4 shRNA constructs	RNAi Consortium, Sigma	Cat# TRCN0000021425 and TRCN0000021426
Software and Algorithms		
CalcuSyn	BioSoft	http://www.biosoft.com/w/calcusyn.htm
Bowtie2 v2.2.4	Langmead and Salzberg 2012	https://sourceforge.net/projects/bowtie-bio/files/bowtie2/2.2.4/
PicardTools	Broad Institute	https://broadinstitute.github.io/picard/
Bedtools	Quinlan and Hall 2010	https://github.com/arq5x/bedtools2

(*Continued on next page*)

Continued

REAGENT or RESOURCE	SOURCE	IDENTIFIER
HOMER	Heinz et al., 2010	http://homer.ucsd.edu/homer/
Tophat2 v2.0.13	Kim et al., 2013	https://ccb.jhu.edu/software/tophat/index.shtml
featureCounts	Liao et al., 2014	http://bioinf.wehi.edu.au/featureCounts/
Rank ordering of super-enhancers (ROSE)	Lovén et al., 2013	https://bitbucket.org/young_computation/rose

CONTACT FOR REAGENT AND RESOURCE SHARING

Further information and requests for resources and reagents should be directed to and will be fulfilled by the Lead Contact, Michelle Monje (mmonje@stanford.edu) with the exception of the VUMC-DIPG-10 line as it was obtained with a standard institutional material transfer agreement (MTA) through Esther Hulleman (e.hulleman@vumc.nl) at the VU University Medical Center. SU-DIPG and SU-pcGBM2 cells will be distributed through the Monje lab with an MTA with Stanford University.

EXPERIMENTAL MODEL AND SUBJECT DETAILS

Patient-Derived DIPG Cell Cultures

All human cell cultures were generated with informed consent and in compliance with Institutional Review Board (IRB)-approved protocols. Patient-derived primary DIPG cell culture models (SU-DIPG-IV: H3.1-K27M; SU-DIPG-VI/XIII-P, JHH-DIPG1, SF7761: H3.3-K27M) have been previously described (Grasso et al., 2015; Hashizume et al., 2012; Table S1). SU-DIPG-XIII-FL cells were cultured at the time of autopsy from a frontal lobe metastasis in subject SU-DIPG-XIII (Table S1). The pontine tumor from subject SU-DIPG-XIII, also cultured at the time of autopsy, is named SU-DIPG-XIII-P. VUMC-DIPG-10 (Table S1) was similarly derived at the time of autopsy. JHH-DIPG1 cells were provided by Dr. Eric Raabe at Johns Hopkins University; SF7761 cells were provided by Dr. Rinataro Hashizume and Dr. C. David James at Northwestern University. SU-DIPG cultures were generated in the Monje Laboratory at Stanford University. SU-DIPG-XVII and SU-DIPG-XXV are newly established H3.3-K27M DIPG primary cell culture derived from DIPG autopsy tissue. All cultures are grown as tumor neurospheres in Tumor Stem Media (TSM) consisting of DMEM/F12 (Invitrogen, Carlsbad, CA), Neurobasal(-A) (Invitrogen, Carlsbad, CA), B27(-A) (Invitrogen, Carlsbad, CA), human-bFGF (20 ng/ml) (Shenandoah Biotech, Warwick, PA), human-EGF (20 ng/ml) (Shenandoah, Biotech, Warwick, PA), human PDGF-AB (20ng/ml) (Shenandoah, Biotech, Warwick, PA) and heparin (10 ng/ml). Histone mutational status was determined using Sanger sequencing for the *H3F3A* and *HIST1H3B* genes. Cell cultures were validated by DNA fingerprinting using short tandem repeat (STR) analysis (Table S2) and checked for mycoplasma contamination. STR fingerprinting is performed on all cultures routinely every ~3 months to confirm veracity of cultures.

DIPG Orthotopic Xenograft Model and Drug Testing

All animal procedures were performed with APLAC approval and adhered to the NIH guide for the care and use of laboratory animals. Both male and female animals were used equally. Animals were randomized to control and treatment groups such that each group had equivalent distribution of initial tumor sizes.

Patient-derived pontine DIPG xenografts were performed as previously described (Grasso et al., 2015). Briefly, a single cell suspension was made from DIPG neurospheres and cells were injected stereotactically into the fourth ventricle/pons of NOD-SCID-IL2 gamma chain-deficient cold-anesthetized mouse pups on postnatal day 2 (P2) or isfluorane-anesthetized mice on P43. SU-DIPG-VI and SU-DIPG-XIII-FL xenografts were performed on P2 mouse pups through a 31-gauge burr hole (coordinates: 3 mm posterior to lambda suture and 3 mm deep) using 100,000 cells in 2 μL total volume. SU-DIPG-XIII-P* xenografts were performed on postnatal day 43 (P43) mice through a 26-gauge burr hole (coordinates: 0.8 mm to right of midline, 0.5 mm posterior to lambda and 5 mm deep) using 400,000 cells in 2 μL total volume.

Administration of THZ1 was performed systemically with intravenous tail vein or intraperitoneal injection (as indicated) five days per week (M-F) at 10 mg/kg. THZ1 stock solutions were dissolved in DMSO at 10 mg/mL and dilute to 1 mg/mL in dextrose (5%) before administration.

For IVIS imaging analyses of in vivo DIPG tumor growth, animals were imaged at baseline and excluded if no tumors were present. For survival studies, morbidity criteria used were either: reduction of weight by 20% initial weight, or severe neurological motor deficits consistent with brainstem dysfunction (i.e. hemiplegia or an incessant stereotyped circling behavior seen with ventral midbrain dysfunction).

METHOD DETAILS

Cell Viability and Combinatorial Drug Synergy

JQ1, panobinostat, OTX015, iBET762, AZD8055, and SCH772984 were purchased from Selleckchem (Houston, TX, USA). THZ1 and LDN-211904 were purchased from Millipore (Billerica, MA, USA). For cell viability measurement, cells were plated into 96-well plates

in at least triplicate and then subjected to drug treatment as indicated. Cell viability was then measured by using Celltiter Glo assay (G7571, Promega, WI, USA), and data were collected on a TECAN Infinite 200 plate reader. For testing combinatory effects of two drugs, the cells were treated with each drug individually or in combination before subjecting to Celltiter Glo assay. CalcuSyn software (Biosoft, Cambridge, UK) was used to calculate the combination index (CI). CI less than 1.0 was considered to be synergistic.

Proliferation, Apoptosis, and Cell Cycle Assays

Cell proliferation and cell cycle phase was measured by using the Click-iT EdU Alexa Fluor 488 or 647 Flow Cytometry Assay Kit (Invitrogen, CA, USA). EdU+ population represented the proliferating cell population. Cell apoptosis was measured by using Annexin V-FITC Apoptosis Detection Kit II (556570, BD Biosciences, CA, USA) with some minor modifications. DAPI was used instead of PI. Cell cycle analysis additionally used LIVE/DEAD Near-IR (Life Technologies, L10119) to mark dead cells and DAPI to label nuclei after fixation and permeabilization. FACS analyses were performed by using BD Fortessa FACS machine (BD Biosciences, CA, USA). The data were analyzed using Flowjo software (FlowJo, LLC, OR, USA).

Lentivirus Preparation and Infection

Two shRNA expressing lentiviral constructs against human BRD4 (TRCN0000021425 and TRCN0000021426) from the RNAi consortium human collection were purchased from Sigma. Lentiviral particles were generated by co-transfection of lentiviral expressing constructs with packaging plasmids (pDelta 8.92 + VSV-G) into 293T cells, and then concentrated by polyethylene glycol (PEG) precipitation method. For lentiviral infection, dissociated DIPG cells were incubated with shRNA expressing lentivirus for 16 h before replacing with fresh medium. Puromycin (0.5 ug/ml) was added to select positively infected cells for further experiments at 48 hours post infection. For in vivo xenograft experiments, no puromycin selection was performed.

Western Blotting

Cells were lysed in RIPA Buffer with 1mM PMSF, protease inhibitor cocktail, 1mM sodium orthovanadate, (Santa Cruz Biotechnology sc-24948) and protein concentration was calculated using Pierce™ BCA™ Protein Assay (Thermo Scientific™). Samples were diluted with 1 volume to 2X Laemmli Sample Buffer (Novex), 20% 2-mercaptoethanol. Gel electrophoresis was performed using SDS-PAGE and proteins were transferred to Immun-Blot PVDF Membrane (BioRad) using Mini-PROTEAN Tetra Cell (BioRad). Membranes were incubated with following primary antibodies for 16-20 hours at 4°C: RNAPII (1:100, Santa Cruz Biotechnologies #sc-899), RNAPII-CTD-SER2 (1:10,000, Bethyl #A300-654A-M), RNAPII-CTD-SER5 (1:2000, Bethyl #A304-408A-M), RNAPII-CTD-SER7 (1:500, Cell Signaling 13780S), CDK7 (1:10,000, Bethyl #A300-405A), Beta-Actin (1:2000, Cell Signaling #4970S), BRD4 (1:5000, Bethyl #A301-985A100), Beta-Tubulin (1:5000, Abcam #ab6046).

LC-MS/MS Analysis of Tissue and Serum Concentration

Tissues samples were weighed and 1 volume of bullet blender beads (Next Advance) and 3 volume of Milli-Q water were added. Tissues were homogenized by a bullet blender (Next Advance) at 4°C according to manufacturer's instruction. The neat stock solutions of THZ1, its internal standard (IS) mutant-EGFR-inhibitor (ChemScene, Cat. No.: CS-2099), OTX015 and its IS CPI-203 (ApexBio, Cat. No.: B1081) were prepared in DMSO and further diluted in 50% methanol to prepare spiking solutions. For spiked standard curve, 25 μl of THZ1 spiking solutions (5 ng/ml- 500 ng/ml) or OTX015 spiking solutions (1 ng/ml- 500 ng/ml) was mixed with 25 μl of their corresponding IS (100 ng/ml) and 25 μl of blank tissue homogenate or serum. For samples, the spiking solution was replaced by 25 μl of 50% methanol to make up the volume. After vortexing all standards and samples, 150 μl of methanol/acetonitrile 20:80 (v/v) was added to the mixture and vortexed vigorously for 1 min followed by centrifugation at 3,000 g for 10 min. The supernatant was diluted 3 times with Milli-Q water.

The LC-MS/MS system consists of a QTRAP 4000 mass spectrometer (AB SCIEX) coupled to a Shimadzu UFLC system. LC separation was carried out on a Dionex C18 column (100 mm × 2.1 mm, 5 μm) at room temperature for both compounds. The analysis time was 2 min. The injection volume was 10-25 μl. For THZ1, isocratic elution was carried out with a mobile phase composed of 35% water and 65% acetonitrile with 0.1% of formic acid and 5 mM of ammonium acetate and a flow rate of 0.3 ml/min. For OTX015, isocratic elution was used with a mobile phase composed of 30% water and 70% acetonitrile with 0.1% of formic acid and a flow rate of 0.4 ml/min. The mass spectrometer was operated in the positive mode with multiple-reaction monitoring (MRM). The following MRM transitions were used: THZ1 (m/z 566.2→186.0), IS for THZ1 (m/z 520.4→72.0), OTX015 (m/z 492.3→383.1) and IS for OTX015 (m/z 400.2→383.1). Data acquisition and analysis were performed using the Analyst 1.6.1 software (AB SCIEX).

ChIP and Library Preparation

Cells were fixed with 1% formaldehyde for 10 minutes at room temperature. Cross-linking was quenched using 0.125 M glycine for 10 minutes before cells were washed twice with PBS. Cross-linked pellets were frozen with dry-ice ethanol and stored at -80°C. Two biological replicates were collected for each cell culture.

Pellets were thawed on ice before cell membrane lysis in 5 mL LB1 (50 mM HEPES pH 8.0, 140 mM NaCl, 1 mM EDTA, 10% glycerol, 0.5% NP-40, 0.25% Triton X-100, 1 mM PMSF, Roche protease inhibitors 11836170001) by rotating for 10 min at 4°C. Nuclei were pelleted at 1350xg for 5 minutes at 4°C. Nuclear lysis was performed in 5 mL LB2 (10 mM Tris-Cl pH 8.0, 5 M, 200 mM NaCl, 1 mM EDTA, 0.5 mM EGTA, 1 mM PMSF, Roche protease inhibitors) by rotating for 10 min at room temperature. Chromatin was pelleted at 1350xg for 5 minutes at 4°C and resuspended in 1.5 mL LB3 (10 mM Tris-Cl pH 8.0, 100 mM NaCl, 1 mM EDTA,

0.5 mM EGTA, 0.1% Na-Deoxycholate, 0.5% N-lauroylsarcosine, 0.1% SDS, 1 mM PMSF, Roche protease inhibitors). Sonication was performed in a Bioruptor Plus until chromatin was 200-700 bp. Debris was pelleted by centrifugation at 16,500xg for 10 minutes at 4°C. Supernatant was collected and Triton X-100 was added to 1% final concentration. Ten percent of sample was collected as input controls. Antibody targeting H3K27Ac (Active Motif #39133) was added at 5 μg per IP to sonicated lysate and rotated at 4°C for 16-20 hours.

Protein G Dynabeads (100 μL per IP) were washed 3x with Block Solution (0.5% BSA in PBS). Antibody bound chromatin was added to beads and rotated 2-4 hours at 4°C. Bead bound chromatin was washed 5x with 1 mL RIPA Wash Buffer (50 mM HEPES pH 8.0, 500 mM LiCl, 1 mM EDTA, 1% NP-40, 0.7% Na-Deoxycholate) then 1x with 1 mL TE Buffer (10 mM Tris-Cl pH 8.0, 1 mM EDTA) with 500 mM NaCl. Beads were resuspended in 210 μL Elution Buffer (50 mM Tris-Cl pH 8.0, 10 mM EDTA, 1% SDS) and chromatin was eluted at 65°C for 15 minutes. Beads were magnetized and supernatant was removed to a fresh tube. Immunoprecipitated and input control chromatin was reverse cross-linked at 65°C for 12-16 hours.

Samples were diluted with 1 volume TE Buffer. RNA was digested using 0.2 mg/mL RNase A (Qiagen 19101) for 2 hours at 37°C. $CaCl_2$ was added to 5.25 mM and samples were treated with 0.2 mg/mL Proteinase K (Life Technologies EO0491) for 30 minutes at 55°C. One volume Phenol-Chloroform-Isoamyl alcohol was added and centrifuged 16,500xg for 5 minutes to extract DNA, followed by a second extraction using 1 volume pure chloroform. Aqueous phase was removed and DNA was precipitated using 2 volumes ethanol and 0.3 M Na-acetate. DNA pellets were resuspended in EB.

To prepare libraries for sequencing, DNA was end repaired using T4 polymerase (New England Biolabs M0203L), Klenow fragment (NEB M0210L), and T4 polynucleotide kinase (NEB M0201L) for 30 minutes at 20°C. 3' A-tailing was performed using Exo- Klenow fragment (NEB M0212L) for 30 minutes at 37°C. Illumina TruSeq Pre-Indexed Adaptors (1 μM) or NEBNext Illumina Multiplex Oligo Adaptors (NEB E7335S) were ligated for 1 hour at room temperature. Unligated adapters were separated by gel electrophoresis (2.5% agarose, 0.5X TBE) and ligated DNA was purified using a NucleoSpin Gel Clean-up Kit (Macherey-Nagel 740609.250). Ligated DNA was PCR amplified using TruSeq Primers 1.0 and 2.0 or NEBNext Multiplex Primers and purified using AMPure XP beads (Beckman Coulter A63881). Purified libraries were quantified using Agilent 2100 Bioanalyzer HS DNA and multiplexed in equimolar concentrations. Sequencing was performed using an Illumina NextSeq or HiSeq at 2x75 bp by Stanford Functional Genomics Facility.

RNA Sequencing

All treatment conditions were collected in biological duplicate. Cells were lysed in Trizol reagent and frozen at -80°C. ERCC spike-in controls were added according to kit guidelines (Thermo 4456740). Total RNA was extracted using chloroform extraction followed by ethanol precipitation and quantified using Qubit.

Selection for polyadenylated (polyA+) RNA was performed using Ambion Dynabeads mRNA Purification Kit (Life Technologies 61006). Briefly, 2.5 μg per sample of total RNA was used for each isolation. Secondary structure was disrupted at 65°C. Ambion oligo(dT) beads were washed twice with Binding Buffer (20 mM Tris-Cl pH 7.5, 1 M LiCl, 2 mM EDTA) then incubated with total RNA. Bound RNA was washed twice with Washing Buffer B (10 mM Tris-Cl pH 7.5, 0.15 M LiCl, 1 mM EDTA) before elution in 10 mM Tris-Cl pH 7.5 at 80°C. Purified RNA was purified once more with oligo(dT) beads as described above and eluted in 10 μL 10 mM Tris-Cl pH 7.5. Purified polyA+ RNA was fragmented using Fragmentation Buffer (Ambion, #AM8740) to 150-400 bp and ethanol precipitated. Fragmented polyA+ RNA was resuspended in water. cDNA was synthesized using Random Hexamer Primers (Invitrogen, #48190-011) and SuperScript II (Invitrogen, #18064-014). Second strand synthesis was performed using DNA Pol I (Invitrogen #18010-025) and RNA was removed using RNaseH (Invitrogen #18021-014). DNA was purified using MinElute PCR Purification Kit (Qiagen, #28004).

Libraries were prepared for sequencing with end repair and A-tailing as described above. NEBNext Illumina Multiplex Oligos were used for indexing and samples were pooled in equimolar amounts. Sequencing was performed using an Illumina NextSeq or HiSeq.

Boyden Chamber Invasion Assays

Invasion of the primary cultures was determined using Biocoat™ Matrigel Invasion Chambers (8.0μm pore size, Corning biosciences). Briefly, dissociated cells were resuspended in growth factor free media and added to the upper chamber of the Transwell insert (0.5-2x10^5 cells/well) along with media containing either DMSO or inhibitor (3 replicates). The lower chamber was filled with stem cell media (2x standard growth factor concentration), with the addition of either DMSO or inhibitor. The assay was allowed to incubate for 72 hours at 37°C, 5% CO_2, 95% humidity. Non-invading cells in the upper insert were removed and cells that had invaded into the lower matrigel surface were fixed with 4% paraformaldyde and stained with 0.1% crystal violet/10% methanol. Crystal violet stained cells were collected using 10% acetic acid from the matrigel surface and measured at an absorbance of 595nm on a NanoDrop spectrophotometer. Relative invasion for each biological replicate was calculated as the fraction of mean LDN-211904 absorbance of all technical replicates over the mean DMSO absorbance of all technical replicates.

3D Migration and Invasion Assays

3D invasion assays were adapted from methods previously described (Vinci et al., 2015). Briefly, cells were seeded at 2x10^3/100 μl/well in ULA 96-well round-bottomed plates (Corning biosciences) and incubated at 37°C, 5% CO_2, 95% humidity to facilitate spheroid formation. After four days incubation, 50ul of media per well was removed and 50 μl of matrigel (Corning biosciences) was added to neurospheres of approx. 200-300 μm in diameter (12 replicates), then incubated at 37°C for 1hr. Once the matrigel solidified, 50 μl/well of stem-cell culture medium containing either DMSO or inhibitor (3x final concentration) was added on top.

Starting from time zero, and at 24-hour intervals up to 72 hours images were collected using standard exposure and gamma settings. The degree of cell invasion into the matrigel was quantifed by 6 diameter measurements using Image J and the data plotted as the average distance of invasion.

3D migration assays were similarly performed as previously described (Vinci et al., 2013), with additional modifications. Briefly, cells were seeded at 10^3/200ul/well in ULA 96-well round-bottomed plates and incubated for four days at 37°C, 5% CO_2, 95% humidity to facilitate spheroid formation. Flat-bottomed 96-well plates (Corning biosciences) were coated with 125 μg/ml matrigel in stem-cell media. Once coating was completed, 200 μl/well of culture medium containing either DMSO or inhibitor (1.5x final concentration) was added to each well. After removal of 100 μl medium from the ULA 96-well round-bottomed plates containing neurospheres of 250-300 μm in diameter, the remaining medium including the neurosphere was transferred onto the pre-coated plates (12 replicates).

QUANTIFICATION AND STATISTICAL ANALYSIS

Statistical Analyses

Bioinformatics methods are described below. IC_{50} values were determined by a nonlinear best-fit method using GraphPad Prism.

The sample size for in vivo experiments was based on variance estimated from experiments with control animals orthotopically xenografted with DIPG cells showing a standard deviation of approximately 30% of the mean. Sample size calculations to detect a 50% difference in tumor growth between two groups with an alpha of 0.05 and a power of 0.8 indicate a minimum group size of 3 animals.

Two-tailed t tests with Tukey or Sidak correction as indicated for multiple comparisons were used for in vitro experiments. A two-tailed t-test was used for comparison of tumor growth rate in orthotopic xenograft experiments. A log-rank test was used for orthotopic xenograft survival analysis.

Outlying data points (>2 standard deviations from the mean in either direction) were excluded. Variance was similar between groups compared.

ChIP-seq Analyses

SU-DIPG-VI and SU-DIPG-XIII-P datasets were generated from 1% DMSO treated cells paired with single and combination treated used for subsequent analysis. SU-DIPG-IV and SU-DIPG-XVII datasets were generated from untreated cells. All datasets were generated in biological duplicate. ChIP-seq datasets were aligned to hg19 annotation of the human genome using bowtie2 (Langmead and Salzberg, 2012) (version 2.2.4). PCR duplicates were removed using Picard Tools MarkDuplicates and bigWigs were generated using UCSC bedGraphToBigWig. Genome tracks were generated using UCSC genome browser (http://genome.ucsc.edu/) with tracks normalized to 1 million reads.

H3K27Ac peaks were called over input controls with full depth libraries using MACS2 (version 2.7.5) with default settings. Enhancers were called as H3K27Ac peaks greater than 2 kb from a TSS, as defined by RefSeq gene annotations. Super-enhancers were identified using ROSE (Lovén et al., 2013) (https://bitbucket.org/young_computation/rose) where enhancers within 12.5 kb were joined together. All enhancers were ranked by density of reads in H3K27Ac ChIP over reads in input.

The nearest RefSeq TSS to each super-enhancer was found using HOMER (Heinz et al., 2010) annotatePeaks.pl. In order to identify potential therapeutic target proteins, microRNAs and snoRNAs were removed from the RefSeq gene annotation. Gene expression values used for associated genes were from DMSO treated control, as described below. Super-enhancer interval overlaps were performed using bedtools (Quinlan and Hall, 2010) and the set of shared super-enhancers was created by joining overlapping super-enhancers with bedtools merge. Gene ontology was performed using GREAT (McLean et al., 2010) and binomial FDR adjusted p values were reported. Pathway analysis was performed using PANTHER (Mi et al., 2016) and Bonferroni adjusted p values were reported.

All libraries were down-sampled to 20 M unique reads for enrichment and signal analyses. Enrichment was calculated by creating tag directories and coverage using HOMER makeTagDirectory and annotatePeaks, respectively, and signal over input was defined as the difference in coverage between H3K27Ac ChIP-seq and input control. Random genomic intervals for super-enhancer comparison were created using bedtools random to match number of super-enhancers and median super-enhancer length for each culture.

Signal at genomic regions was measured by using bedtools coverage to count ChIP-seq reads within regions. H3K27Ac signal was defined as the difference in number of reads in H3K27Ac ChIP-seq and reads in input controls. Density was then calculated as the signal divided by the length of the region in kilobases. For comparison of replicates and differential testing, DESeq2 was used and scatter plots were generated in R using smoothScatter. Distance of H3K27Ac regions to TSS was determined using bedtools closest.

Gene Expression Analyses

Reads were mapped to hg19 annotation using Tophat2 (Kim et al., 2013) (version 2.0.13) and duplicates were removed using Picard Tools. ERCC spike-in reads were mapped using bowtie2 alignment an ERCC reference. Transcript coverage of RefSeq gene annotations and ERCC spike-in counts were performed using featureCounts (Liao et al., 2014). Differential testing and log2 fold change calculation was performed using DESeq2 (Love et al., 2014) with two biological replicates and FDR=0.1, with normalization calculated on only the set of ERCC spike-in counts. Primary tumor analysis was performed on all SU-DIPG samples published in Grasso et al., 2015.

Active transcripts were defined as genes with a mean FPKM of at least 5 in DMSO controls. Unsupervised hierarchical clustering was performed on the top 10% of downregulated panobinostat and JQ1 transcripts and top 5% of THZ1 downregulated transcripts active in both cultures using heatmap.2 from R package gplots. Gene Ontology was performed using GO Consortium (Ashburner et al., 2000) and pathway analysis by PANTHER (Mi et al., 2016). Violin plots were generated using ggplot2 of log transformed (FPKM+1) values.

Gene set enrichment analysis (GSEA) of drug-treated DIPG cells was performed as previously described (Grasso et al., 2015) (www.broadinstitute.org/software/gsea) (Subramanian et al., 2005) by using two customized DIPG super-enhancer (SE) related gene sets. These two gene sets, TANG_ACTIVESE_DIPG6 and TANG_ACTIVESE_DIPG13, contained actively transcribed SE-associated genes in SU-DIPG-VI and SU-DIPG-XIII-P cell cultures respectively. Normalized Enrichment Score (NES) and FDR q-value were calculated by using permutation type of gene-set. Significantly enriched gene sets were called by using cut-off of FDR $\leq$ 0.1

3D Migration and Invasion Quantification

Starting from time zero, and at 24-hour intervals up to 72 hours, images were collected using standard exposure and gamma settings. The degree of cell spread on the matrix was measured using Image J and relative invasion plotted as the average distance of migration as a ratio to distance at 0 days.

DATA AND SOFTWARE AVAILABILITY

All RNA and ChIP sequence data are available through GEO (GSE94259).

ADDITIONAL RESOURCES

Not applicable